Near Infrared Spectroscopy for measuring Optical Parameters in Flour and Grain

---

Viveka Anderberg

Master's thesis
Lund University
Faculty of Engineering, LTH
June 2009

Abstract

This master's thesis project is performed in cooperation between the Division of Atomic Physics, Lund University, and the Danish company FOSS. The purpose of the project was to investigate the optical properties of some flour and grain samples, for which FOSS develops instruments. This was accomplished by using time-of-flight spectroscopy, which means that light is sent into the sample in one point, and detected in another. Depending on the optical properties of the material, different amounts of light will be absorbed, i.e. it will not reach the detector, or scattered, i.e. it will change direction inside the sample. By analysing the detected light it is possible to draw conclusions about the physical and chemical properties of the material.

The data obtained with time-of-flight spectroscopy was used in simulations of existing instruments manufactured by FOSS, constructed to analyse this kind of samples. Reference data was produced with the FOSS instruments and the goal was to get a simulation to produce the same output as the real instrument. If the matching between reality and simulation was good enough, FOSS would be able to use simulations to evaluate changes and reconstructions of their instruments. Today they are forced to rebuild the instruments and to perform large amounts of test measurements in order to find for example the most optimal dimensions of an instrument. By using a simulation instead, much time and effort could be saved.

The conclusion after having compared the simulations with the reference data was that the flour behaved rather good, but still details in the measurement method and the sample preparation caused small deviations in the result. This left the simulations not yet as good as required to be used as a complementary method in the construction process of an instrument. The grains were very large, and the time-of-flight technique is not developed to handle this kind of material, resulting in bad conditions from the beginning. Despite that the final result turned out, not perfect, or good, but certainly better than expected.

Sammanfattning

Det här examensarbetet är utfört i samarbete mellan avdelningen för Atomfysik på Lunds Tekniska Högskola och det danska företaget FOSS. FOSS bildades 1956 av Nils Foss som använde spektroskopi för att bestämma fukthalten i spannmål. Så småningom växte företaget och idag är det världens största leverantör av analytiska testinstrument till både jordbruk, läkemedels-, livsmedels-, och kemibranschen. Medicingruppen på Atomfysik inriktar mycket av sin forskning mot att använda optik i biomedicinska sammanhang. Exempel på forskningsområden är att utveckla metoder för att undersöka eller behandla mänsklig vävnad, men också att med spektroskopi analysera t.ex. läkemedel i tablettform.

Syftet med det här projektet har varit att med hjälp av spektroskopiska metoder undersöka optiska parametrar för ett par av de spannmålstyper som FOSS tillverkar analysinstrument för. Detta kan man göra genom att använda så kallad *tidsupplöst spektroskopi*, vilket går ut på att man skickar in ljus i provet och sedan detekterar det ljus som kommer ut igen. Beroende på provmaterialets egenskaper så kommer olika mycket ljus att absorberas, dvs. inte komma ut igen, och spridas, dvs. ändra riktning inne i provet.

Genom att utnyttja tidsupplöst spektroskopi kan både absorptionen och spridningen i provet bestämmas, dessa kan sedan ge information om provets kemiska och fysikaliska egenskaper. Tillvägagångssättet är att en mycket kort laserpuls skickas in i provet genom en optisk fiber. Inne i provet kommer ljuset att till största delen att spridas ett stort antal gånger innan det når en annan optisk fiber som finns på andra sidan provet och som leder ljuset till en detektor. Detta resulterar i tidiga och sena fotoner, dvs. en del fotoner tar en ganska rak väg genom provet och kommer fram snabbt, medan andra färdas betydligt längre och kommer fram senare. På så sätt får man en fördelning i tiden från den första snabba fotonen, till den sista långsamma, vilket visas i Figur 1.

Mätningarna gick ut på att fastställa provernas absorberande och spridande förmåga, för att sedan använda dessa värden i simuleringar av de instrument som FOSS utvecklar. Syftet var att få samma slutresultat som man får genom att mäta

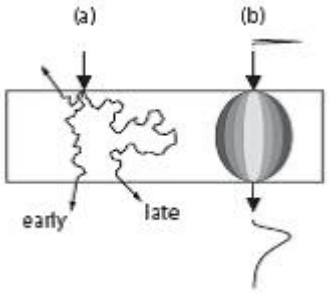

Figur 1: *a) Tidiga fotoner går ganska rakt genom provet och kommer snabbt fram till detektorn, medan de långsamma sprids fler gånger och når detektorn senare. En del fotoner förloras helt eftersom de lämnar provet på andra ställen än där detektorfibern är placerad.*
b) Den korta pulsen breddas genom att fotonerna tar olika lång tid på sig att passera genom provet. Det detekterade resultatet blir därför en kurva med större utsträckning i tiden. [1]

med de verkliga instrumenten. Om resultaten skulle visa sig stämma överens med resultaten från FOSS-instrumenten skulle det vara möjligt att genom att endast använda simuleringar ta reda på hur resultatet från ett tjockare/tunnare prov, eller ett prov som flyttats i sidled, skulle se ut. FOSS skulle då inte behöva modifiera sina instrument och göra ett stort antal testmätningar när de vill förändra eller optimera sina lösningar.

Det slutliga resultatet, att jämföra en mätning med ett FOSS-instrument med en simulering, stämde överkomligt bra överens med varandra. De båda spektran för okompromerat mjöl följer samma form, men de absoluta värdena stämmer inte exakt överens överallt, vilket kan ses Figur 2. För hela korn- och vetekorn blev resultatet inte lika tillfredsställande. De simulerade kurvorna har former som liknar de verkliga, men de absoluta värdena stämmer bara överens i ett fåtal punkter. De båda kurvorna för korn visas i Figur 3, och de för vete i Figur 4.

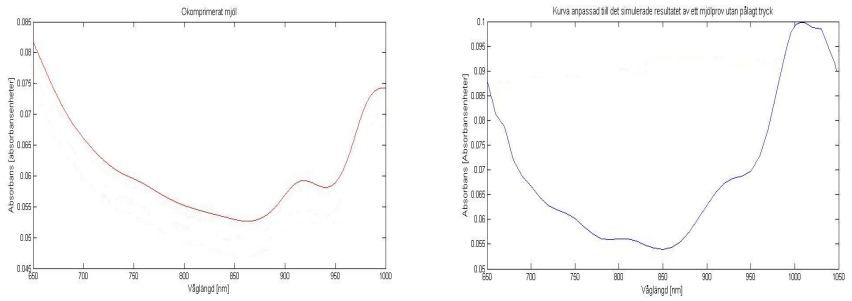

Figur 2: *Till vänster resultatet av en mätning med ett FOSS-instrument, och till höger från en simulering, båda framtagna med okomprimerade mjölprover.*

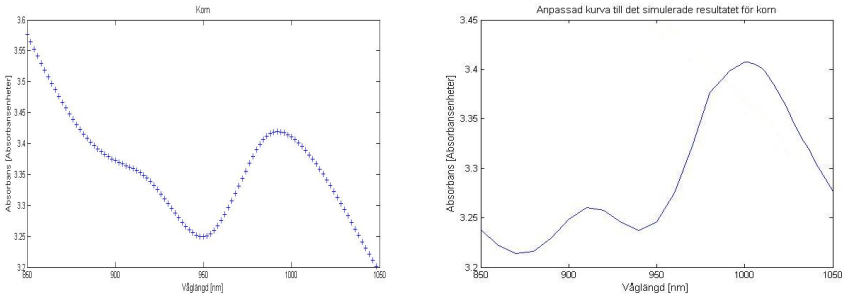

Figur 3: *Till vänster visas absorbansspektrat för korn uppmätt med FOSS-instrumentet, och till höger det simulerade resultatet.*

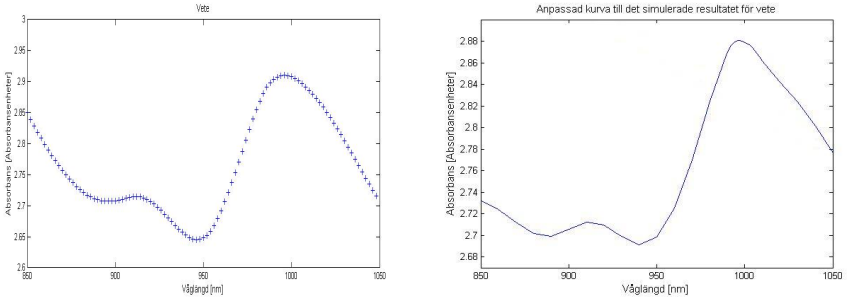

Figur 4: *Till vänster visas den med FOSS instrument uppmätta absorbanskurvan för vete, och till höger det simulerade resultatet.*

Contents

Chapter 1

Introduction

1.1 Background

The project behind this Master's Thesis was performed in cooperation between FOSS, Höganäs, and the Department of Atomic Physics, Lund Institute of Technology.

FOSS is a Danish company founded in 1956 by Nils Foss and the first instrument developed had the ability to measure moist content in grain. The company grew to also include analytical instruments for testing, among others, dairy, meat and pharmaceuticals.

FOSS has now been in the business for more than 50 years and is the leading provider of analytical instruments for the food, agricultural, pharmaceutical and chemical industries. The costumers are spread out over 22 countries and 85% of the world's milk production, and 80% of the grain production is tested with FOSS instruments.

The technologies used range from dual x-rays for meat analysis, and near infrared spectroscopy for measurements of food and liquids, to image analysis for grain inspection, and wet chemical analysis. [2]

The Biophotonics Group at the Department of Atomic Physics in Lund is pursuing their research towards biomedical optics. The area includes e.g. developing methods to monitor or treat human tissue, or analysing e.g. pharmaceutical materials. In order to perform this, methods like Monte Carlo simulations, and different kinds of spectroscopy are frequently used. The time-of-flight spectroscopy method is used for characterization of highly scattering materials such as tissue, pharmaceutical samples, and as was the case in this work, flour. [3]

1.2 Goal

The aim of the work presented in this thesis was to determine the optical properties of both flour and different grains by using the methods provided by the Biophotonics Group at the Department of Atomic Physics, in this case i.e. time-of-flight spectroscopy. The parameters to determine with this technique were the absorption coefficient and the reduced scattering coefficient of different samples of grain and flour. The evaluation was done at a large range of wavelengths, and parameters such as the degree of compression of the samples were varied. The reproducibility of the measurements was an important factor to evaluate, since that determines if the methods would be usable. The same measurements were also performed with instruments from FOSS.

The parameters obtained with time-of-flight spectroscopy were to be used in simulations of FOSS instruments. The aim was to get the same output from the simulations as from the real measurements. If that goal was reached, by only changing parameters in the program, it would be possible to determine what output an instrument would give if a sample would be thicker or thinner than normal, if the light source is changed or if the sample is placed out of its correct position in the instrument. This would give FOSS the opportunity to make simulations instead of modifying their instruments and perform a lot of test measurements when they want to evaluate or optimize their products.

1.3 Outline

Chapter 2 in this thesis starts with the background theory of light propagation in turbid materials, where the optical properties and different kinds of scattering are explained. The radiative transfer equation and the diffusion equation are also described as well as methods of how to solve them. In this chapter the time-of-flight spectroscopy method and the experimental setup are also described. Chapter 3 presents the technique of time-of-flight spectroscopy, followed by simulations of FOSS instruments in Chapter 4, and a brief explanation of the FOSS instruments that have been used in Chapter 5. The results of the work are found in Chapter 6, and in Chapter 7 some conclusions, a look at the future and a further development of the project.

Chapter 2

Theory

2.1 Light Propagation in Scattering Media

2.1.1 Introduction

The theory of light propagation in turbid materials is based on the assumption that the photons act as particles, and the wave properties of the light are thus neglected. The result, the linear transport theory, was originally developed to model neutron propagation in nuclear processes. It is based on the two events scattering and absorption, which makes it suitable to use also for light propagation modelling.

2.1.2 Optical Properties

The absorption of light in a material is determined by the Beer-Lambert's law:

$$I = I_0 exp(-\mu_a L) \tag{2.1}$$

where I is the light intensity transmitted through the sample, I_0 is the intensity of the incident light, μ_a is the absorption coefficient and L is the path length through the material. The absorption coefficient, μ_a $\left[cm^{-1}\right]$, expresses the probability for a photon to be absorbed per unit path length. The condition for absorption is that the energy of the photon matches the difference between two energy levels in the atom or molecule. If that is the case, an electron in the molecule absorbs the photon energy and is raised to a higher energy level, while the photon is annihilated, or continuous its path with less energy. The latter occur when the energy gap between the two levels is smaller than the initial energy of the photon. The inverse of the absorption coefficient is equivalent to the average path length before absorption in the material.

In turbid materials, scattering is the dominant process over absorption, and the light propagation is thus determined mainly by the scattering coefficient, μ_s $\left[cm^{-1}\right]$. This coefficient gives the probability for a photon to be scattered per unit path length, and the average number of scatterings per unit path length. There are two ways a photon may be scattered, *elastically* or *inelastically*. Elastic scattering signifies that the photon's energy is not changed during the scattering process, while inelastic scattering means that the energy is changed. [4, 5]

2.1.3 Scattering Phase Function

The probability of the photon to be scattered in a certain direction is determined by the scattering phase function, $p(\hat{s}', \hat{s})$. The most common used phase function is the Henyey-Greenstein phase function:

$$p(cos\,\theta) = \frac{(1-g^2)}{2(1+g^2-2g\,cos\,\theta)^{3/2}} \tag{2.2}$$

where $g =< cos\theta >$ is called the g-factor, or the anisotropy, and can vary between -1 and 1. If the value of g is close to 1 the light is mainly scattered in a forward direction, $g = -1$ implies backward scattering, and if the g-value instead is close to 0 the scattering is isotropic. See Figure 2.1. [6] Together, g and μ_s form the reduced scattering coefficient:

$$\mu_s' = (1-g)\mu_s \tag{2.3}$$

This coefficient alone can describe the light propagation process over large spatial distances, which is typically a few millimetres in highly scattering media. [7]

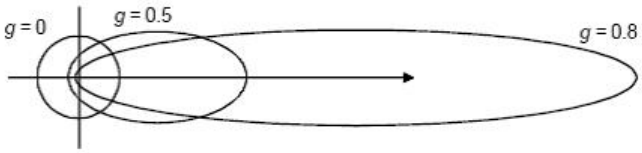

Figure 2.1: *The Henyey-Greenstein phase function for different values of the scattering anisotropy g-factor.* [6]

2.1.4 Rayleigh and Mie Scattering

Light scattering is usually described by geometrical optics with e.g. refraction. But as the scattering particles get smaller, this is not a valid approximation anymore. For scattering particles of the same size or smaller than the wavelength other models are needed. The two main scattering theories for small particles are *Rayleigh* and *Mie* scattering.

In 1897 J.W.S. Rayleigh came up with an approximation of scattering caused by small particles. He figured that the particles are so small compared to the wavelength that what they see is an electric field varying over time. This field induces an oscillating dipole moment in the particle, which will have the same frequency as the incident field, i.e. the light. The dipole will then re-emit the radiation with the same frequency as the incoming light, but isotropically.

Scattering by particles much smaller than the wavelength is thus called Rayleigh scattering and it follows a $\frac{1}{\lambda^4}-$dependence for the scattering cross section.

Through his reasoning Rayleigh could show that shorter wavelengths are scattered more than longer, and by that he was able to explain both the blue sky (short wavelengths), and the red sunsets (long wavelengths). The condition for his theory to be valid is that $r \ll \frac{\lambda}{2\pi}$, where r is the particle radius and λ is the wavelength of the incoming light. [7, 8, 9]

A couple of years after Rayleigh's discoveries, in 1908, G. Mie wrote about scattering caused by particles of the same size as the wavelength of the incident light. One condition for Mie's theory to be valid is that the scattering particles must be spherical. The theory is actually valid for all sizes of spherical particles, but the term Mie scattering is only used for particles approximately the same size as the wavelength. The Mie scattering is, just like Rayleigh scattering, wavelength dependent, following $a\lambda^{-b}$, where a and b are constants, and b is smaller than 4. [7, 9]

2.1.5 The Radiative Transfer Equation

To calculate how the light is distributed in a volume over time the so called Radiative Transfer Equation (RTE) is used. It expresses the energy balance inside an element of scattering media. In the case of absorption, all energy of the photon is considered as lost, e.g. transformed into heat, and in the case of scattering the direction of the photon is changed, but the frequency is considered to remain intact. [10]

To build up the equation a volume V with a boundary area A is considered. The equation consists of the following four terms, see also Figure 2.2 for further explanation:

a. The flow through the boundaries, A, $[m^2]$, of the volume V,$[m^3]$.

b. Absorption, and scattering from the direction of $\hat{s}$.

c. Scattering into the direction of $\hat{s}$.

d. Sources within the volume V, $[m^3]$.

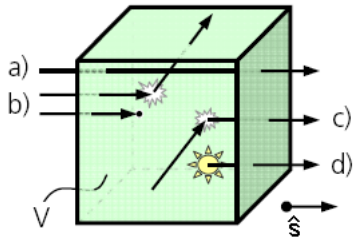

Figure 2.2: *The figure shows the components of the Radiative Transfer Equation. [11]*

The first term in the equation, a), consists of the photons entering or exiting to or from V, via A. The number of photons transferred into or out of V is:

$$\left(\frac{\partial N}{\partial t}\right)^{V}_{transfer} = -\int_{A} cN\hat{s}\cdot\hat{n}\,dA = -\int_{V} c\nabla N\cdot\hat{s}\,dV \tag{2.4}$$

The next term consists of the photons absorbed inside the volume. Since the probability of absorption during the time dt is $\mu_a c dt$, the total number of photons lost due to absorption is:

$$\left(\frac{\partial N}{\partial t}\right)^{V}_{abs} = -\int_{V} c\mu_a(\bar{r})N\,dV \tag{2.5}$$

Photons that are scattered from the $\hat{s}$-direction into another, also means that the photon is lost. This term instead depends on the scattering coefficient:

$$\left(\frac{\partial N}{\partial t}\right)^{V}_{scatt_-} = -\int_{V} c\mu_s(\bar{r})N\,dV \tag{2.6}$$

The photons scattered from all other directions and ending up in the $\hat{s}$-direction, term c), contributes with:

$$\left(\frac{\partial N}{\partial t}\right)^{V}_{scatt_+} = \int_{V} c\mu_s(\bar{r})\left(\int_{4\pi} p(\hat{s}',\hat{s})N(\hat{s}')d\omega'\right)\,dV \tag{2.7}$$

where $p(\hat{s}',\hat{s})$ is the probability that a photon travelling along $\hat{s}'$ is scattered into $\hat{s}$, and $N(\hat{s}')$ the number of photons travelling in the $\hat{s}'$-direction. The last term is the one related to the light source, d), where $q(\bar{r},\hat{s},t)$ describes the number of photons produced per unit volume, steradian and time:

$$\left(\frac{\partial N}{\partial t}\right)^{V}_{source} = \int_{V} q(\bar{r},\hat{s},t)\,dV \tag{2.8}$$

By putting all the terms together, the transfer equation is reached. The integrals may be dropped since the volume is arbitrary. [5, 10]

$$\frac{\partial N}{\partial t} = -c\nabla N \cdot \hat{s} - c(\mu_s + \mu_a)N \; + c\mu_s \int_{4\pi} p(\hat{s}', \hat{s}) N(\hat{s}') d\omega' + q \tag{2.9}$$

For simplicity the source term can be assumed to consist of a point source, described by a Dirac delta function: $q(\bar{r}, \hat{s}, t) = \delta(\bar{r})\delta(\hat{s})\delta(t)$. From this simplification the general solution can be obtained by convolution integrals. [10]

2.1.6 The Diffusion Equation

The transfer equation is impossible to solve analytically in a 3D-geometry, but for other geometries it may be possible to solve, but only when certain conditions are fulfilled. Instead various techniques can be used to solve it numerically, with methods based on approximations and simplifications. One of the most frequently used approximations is the diffusion theory, based on the expansion of spherical harmonics. The expansion is written:

$$L(\bar{r}, \hat{s}, t) = \sum_{l=0}^{\infty} \sum_{m=-l}^{l} \sqrt{\frac{2l+1}{4\pi}} L_{lm}(\bar{r}, t)\, Y_{lm}(\hat{s}) \tag{2.10}$$

With N terms the expansion is ended and the result is called the $P_N -$ approximation, i.e. P_1 when the 0:th and 1:st terms are used and so on. Followed by some additional assumptions regarding the light source and the flux, the diffusion equation is reached:

$$\frac{1}{c}\frac{\partial}{\partial t}\phi(\bar{r}, t) = \nabla D(\bar{r})\, \nabla\phi(\bar{r}, t) - \mu_a \phi(\bar{r}, t) + Q(\bar{r}, t) \tag{2.11}$$

Here, $\tilde{D} = \frac{1}{3(\mu_a + \mu_s(1-g))} = \frac{1}{3(\mu_a + \mu_s')}$ is called the diffusion coefficient. The diffusion equation is only valid under certain circumstances, the light must propagate diffusely, meaning that the reduced scattering coefficient, μ_s', must be much larger than the absorption coefficient, μ_a. The fluence, ϕ, must also be calculated far from the source, allowing the light to become diffuse. These conditions result in a simplification of the diffusion coefficient: $D = \frac{1}{3\mu_s'}$. [12]

2.1.7 Geometries for Solving the Diffusion Equation

The diffusion equation is possible to solve for some simple geometries. The first assumption to make is that the material is homogenous, and then the easiest geometry to start with is an infinite medium with no boundaries. If a continous lightsource $Q(\bar{r}, t) = P_0\delta_r$ is used and the system is supposed to be stationary, the spatially resolved solution of the diffusion equation for this geometry is:

$$\phi(\bar{r}, t) = \phi(r) = P_0 \cdot \frac{3\mu_s'}{4\pi r} exp(-\mu_{eff} r) \tag{2.12}$$

where $\mu_{eff} = \sqrt{3\mu_s'\mu_a}$, $\left[cm^{-1}\right]$, is called the effective attenuation coefficient. Since the fluence depends on both μ_s' and μ_a it is not possible to separate absorption and scattering by spatially resolved measurements.

If instead a pulsed light source is used, $Q(\bar{r},t) = E_0\delta_r\delta_t$, the time resolved solution becomes:

$$\phi(\bar{r},t) = cE_0\left(\frac{3\mu_s'}{4\pi ct}\right)^{3/2} exp\left(\frac{-3\mu_s' r^2}{4ct} - \mu_a ct\right) \tag{2.13}$$

where $c = \frac{c_0}{n}$ is the speed of light in the medium. [13]

The calculations can be extended by inserting boundaries in the geometry; a semi-infinite medium which contains one boundary, or a slab geometry with two boundaries. Since the slab geometry has been used in this work it will be explained in detail.

The slab consists of a thin layer of a turbid medium, with width d and refraction index n_2, surrounded by another medium, with refraction index n_1, see Figure 2.3.

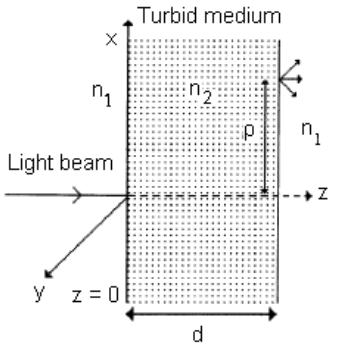

Figure 2.3: *A slab geometry with the light incident on the left side, and the detector a distance r from the z-axis on the opposite side of the slab.* [10]

A narrow, collimated light beam, described by a Dirac delta function, is pulsed into the slab in the direction of the z-axis. The light is then scattered and absorbed inside the slab, until some of it reaches the other side a vertical distance $\bar{r}$ from the z-axis. See Figure 2.3. [10]

The simplest boundary condition of the slab geometry is to assume that the fluence is equal to zero at the boundary between the slab medium and the surrounding medium. To obtain zero fluence, mirror sources are placed on each side of the boundary, or boundaries, in the case of the slab geometry, at a distance of $z = \pm z_0 = \pm\frac{1}{\mu_s'}$.

The problem with this solution is that it is valid only when the two mediums have the same refractive index. For materials with different refractive indices, which usually is the case, Fresnel refraction will occur at the boundary, i.e. the reflection

angle, θ_2, depends on the incoming angle, θ_1, and the two refractive indices, n_1, n_2, as: $n_1 \sin(\theta_1) = n_2 \sin(\theta_2)$. This means that the fluence will in fact not be zero at the boundary, and the boundary condition saying zero fluence turns out to be unphysical.

To compensate for the non-zero fluence at the boundary, a model using extrapolated boundaries is used. In this case an extrapolated boundary is placed a distance $z = z_e = 2z_0 = \frac{2}{\mu_s'}$, outside the turbid medium, or in the case of a slab, one extrapolated boundary on each side of the slab. To obtain zero fluence at the extrapolated boundaries, mirror sources are introduced on each side of them, at a distance of $z = \pm z_0 = \pm\frac{1}{\mu_s'}$. In the slab geometry, mirror sources are of course placed around both extrapolated boundaries. The fluence is then zero at the extrapolated boundary, and non-zero on the real boundary. [14] For further clarity of the arrangement see Figure 2.4.

In the case of a geometry consisting of a thin slab, the two boundaries will affect each other with regard to the internal reflection. It is then necessary to introduce multiple mirror sources, located at

$$\begin{cases} z_{+,m} = 2m(s + 2z_e) + z_0 \\ z_{-,m} = 2m(s + 2z_e) - 2z_e - z_0 \end{cases}$$

for positive and negative sources respectively, where $m = 0, \pm1, \pm2, \ldots$

By adding all fluence contributions from both positive and negative sources the total fluence at a distance $\bar{r}$ from the z-axis is obtained. After a rather great deal of calculations expressions for the time-resolved reflection and transmission can be obtained. The expressions are shown in Appendix A. [10]

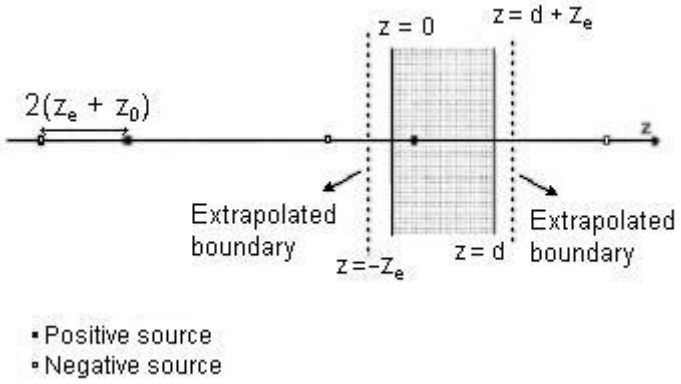

Figure 2.4: *Positions of extrapolated boundaries and source dipoles in a slab geometry. [10]*

2.2 Time-of-Flight Spectroscopy

2.2.1 Introduction

Absorption spectroscopy is used in a wide range of applications and is based on the assumption that light intensity in a medium decays according to Beer-Lambert's law: $I = I_0 exp(\mu_a L)$, and thus only depends on the absorption in the medium. Since absorption is not dominating over scattering in all materials, this assumption will not always be valid. To be able to use the Beer-Lambert law it is also required that the optical path length, L, is known. In a sample where absorption is the strongest optical effect, the path length is known to be the same as the sample width. The detected signal will thus only depend on the sample size, i.e. the larger the sample, the more photons will be absorbed. In the case of scattering being the dominant process, the path length in the sample is instead determined by the scattering coefficient. In that case the detected signal will also depend on the geometry of the sample, causing photons to be lost via borders because of scattering. The sample will still some absorption, but not as outstanding as in the first case.

By using Time-of-Flight Spectroscopy (TOFS) both the reduced scattering coefficient and absorption coefficient may be determined. The phenomena making TOFS possible is that the path of different photons going through a scattering media will be of different lengths. [1] A simplified setup consists of an optical fibre delivering light to the sample. The light is then scattered inside the medium and a small fraction of it reaches the detector, i.e. another optical fibre. The photons may take an infinite number of paths between the source and the detector, but some of the paths are more likely than others. A very unlikely path is one going close to the surface of the sample, because the risk of the photon being scattered out of the medium is high. Paths going deep into the sample before heading for the detector are also unlikely since the probability for the photon to be absorbed is high. The most probable path is then one that follows a direction somewhere in between the two extremes. [15]

The photons scattered mainly in the direction of the detector will be detected earlier than those photons having been scattered around in the whole sample, before reaching the detector. The photons can thus be divided into two groups; early and late, because they have different time-of-flight. By collecting the photons as time goes by, a distribution in time is obtained, which is shown in Figure 2.5. [1]

2.2.2 Setup

Two setups have been used to determine the absorption and reduced scattering coefficients of the samples. The main difference between the setups is that different detectors, PMT:s have been used, one from here and on called the "old" PMT, and one called the "new". The setup with the "old" PMT is shown in Figure 2.7 and with the "new" in 2.10. For both setups the same super continuum laser, *Fianium Tuneable Supercontinuum Source, SC450-AOTF* was used as the light source and the same AOTF-filters was used. All parts of both setups will be explained in detail in the following parts.

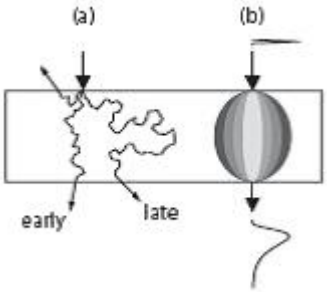

Figure 2.5: *(a) shows different photon paths in a sample. Early photons are not scattered as many times as those arriving later. Photons are also lost due to backscattering in the surface of incidence.*
(b) shows the broadening of a short incident pulse when it travels through a scattering sample. [1]

To reach a high sensitivity of the measurements the *time correlated single photon counting technique* (TCSPC) is used. To be able to make use of the fast laser repetition rate, TCSPC is needed. Without it, the short laser pulses would not be of advantage to the setup.

The Laser

The laser consists of a master source, a high power amplifier, a super-continuum generator and a collimator, shown in Figure 2.6. The master source consists of a core-pumped, Yb-doped, low-power fibre laser. It has a repetition rate of 80 MHz and generates pulses of 6.0 ps. The master source is coupled to an amplifier, a Yb-doped fibre with double cladding. This is pumped by a high power laser diode pumping device. Without the amplifier the laser system would only give an output of a few milliWatts, with a narrow spectral bandwidth centred around 1064 nm. With higher amplification rates both the optical output power and the spectral bandwidth are increased. [16]

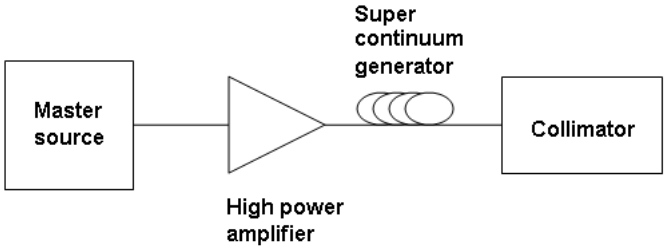

Figure 2.6: *Flowchart of the laser components. [16]*

To generate a broader spectrum a super continuum generator is used. This consists of a highly nonlinear optical fibre, a *photonic crystal fibre* (pcf). This is a

special type of optical fibre with a built-in microstructure. The most common, and also used in this fibre, is small air holes in the glass. By manufacturing the fibre with different hole arrangements, the optical properties of the fibre changes. The air holes change the fibre's waveguide properties, i.e. how the fibre leads the light, because the refractive index changes as the light propagates. [17] The high non-linearity together with the high pulse-peak powers the spectral range of the pulse is broadened to range from 450 to 1750 nm in the fibre. The broadening of the spectra is a non-linear process; the spectra will first be extended to longer wavelengths, i.e. greater than 1064 nm, which in turn will generate the shorter ones, below 1064 nm. With maximum power to the amplifier, the optical output power is 2.5 W.

Acusto Optical Tuneable Filters (AOTF)

The white laser light is transported via an optical fibre to one of two acusto optical tuneable filters (AOTF 1 or AOTF 2). These filters consists of a birefringent (double refractive) crystal, which changes its refractive index when exposed to an acoustic wave. The filter construction is based on the Bragg condition: $\sin\theta = \lambda/2\Lambda$, where θ is the angle of the incoming light, λ is the wavelength of the light, and Λ is the acoustic wavelength. If both the angle θ and the acoustic wavelength Λ are specified, reflection of the incident light can only occur for one single optical wavelength: $\lambda = 2\Lambda \sin\theta$. All the other optical wavelengths present will be refracted in other directions and will eventually disappear.

In this case the refractive index of the crystal is varied by using a piezoelectric transducer to induce an acoustic wave. The optical wave, with wavelength λ, enters the crystal. One wavelength, the one corresponding to the acoustic wavelength, is then selected to be totally reflected through the chrystal. On the other side of the chrystal, the light with the chosen wavelength is collected by a fibre placed in a pinhole. To select another optical wavelength, the frequency of the piezoelectric transducer is changed, to get another acoustic wavelength. [18, 19]

The filters, i.e. the piezoelectric transducers, are controlled by an AOTF-driver, which in turn is controlled through a computer. From the AOTF the one selected wavelength is coupled into an optical fibre, of which the other end is placed in a sample holder. From there the light passes through the sample, where it is scattered, and to some amount, also absorbed. The part of the light that passes through the sample is collected by another optical fibre, the detector fibre, leading it to the detector.

The source and detector fibres can be placed in the holder in two different ways, either next to each other, when measurement in reflectance mode, or on opposite surfaces of the sample, to measure in transmission mode.

The Detectors

After being collected by the detector fibre, the photons pass through an adjustable filter, implemented by a gradient wheel, to obtain optimal signal strength. If too

many photons are removed, the signal will disappear, but if too few are removed the detector may be saturated and destroyed. After passing the adjustable filter the photons will hit a *multi channel plate* (MCP), placed in front of a *photo multiplier tube* (PMT).

Since the detectors must be extremely sensitive to be able to detect single photons, both the MCP and the PMT have to be cooled. The PMT mainly used in this project, the "old" one, is electronically cooled to -30^{o} C, to avoid noise originating from background radiation. In order to detect every single photon the MCP enhances the signal by emitting a large number of photons for every incoming photon. To reach a high sensitivity the TCSPC technique is used. In Figure 2.7 the old setup is shown and in Figure 2.9 the system is shown with the TCSPC-parts included.

When the signal has reached the PMT a signal is sent to a *constant fraction discriminator* (CFD). See Figure 2.9. The CFD reduces the noise in the measurements by excluding signals too high or too low in amplitude, assuming that they originate from the detector or from electronics. A signal is then sent to a *time-to-amplitude converter* (TAC) and a clock is started. When the next laser pulse goes off, a *sync*-signal is sent to the TAC, and this stops the clock. The time interval from the clock started until it is stopped is converted into an electrical pulse, with amplitude proportional to the time span. This pulse reaches the *multi-channel analyser* (MCA) where the right channel, corresponding to the voltage, is increased by one count. Since a very large amount of photons will be detected during a measurement a histogram will eventually be built up. [21, 20]

The width of the channels in the MCA determines the time-resolution of the system, and for this setup, using the old PMT, it is approximately 24.4 ps. The TAC is limited by requiring a certain time, in this case 1 µs, to start, stop and reset. The maximum sampling rate of the TAC is thus 1 MHz.

The method behind the TCSPC-technique is based on statistics, which means that it requires a certain number of photons to be detected to get the resulting curve as good as possible, without noise. The opposite phenomenon is called pile up, and implies that too many photons are reaching the detector. The possibility to detect one photon per excitation pulse is almost equal to 1, leading to a not negligible possibility that two photons reach the detector at the same time. Since the detector can only register one photon at a time, the second one will be lost, which gives rise to an error in the statistics and therefore in the prolongation also in the results. [20]

For the second setup, using the newer PMT; *R3809-U 68 Hamamatsu Photonics*, the same laser, AOTF, AOTF-driver, computer and optical fibres are used, in the same way as before. The detector however, has a PMT built up of InP/InGaAs, instead of Si, which transfers the sensitive area from 650-1050 nm of the old PMT, to 950-1400 nm. Since the detected wavelengths are longer, i.e. contains less energy, the registered noise level will increase. To avoid detecting as much of the noise as possible, the detector is cooled by liquid nitrogen to -80^{o}C to obtain better measurements. The detector has a built-in filter wheel and a shutter, each one controlled by a filter wheel controller and a shutter controller respectively. It is also equipped with a protection circuit coupled to the shutter controller. If too many photons are registered the shutter will be closed immediately to protect the PMT from being saturated. The setup is shown schematically in Figure 2.10.

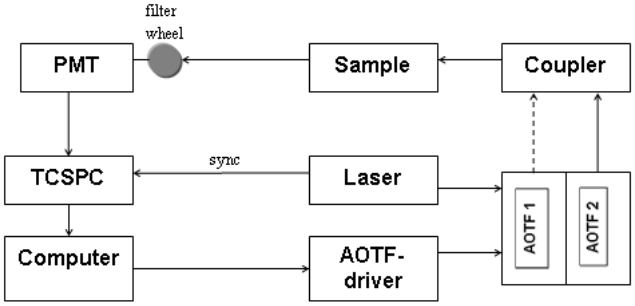

Figure 2.7: *The TOFS setup with the old PMT used for measurement the absorption and reduced scattering coefficients in the flour and grain samples.*

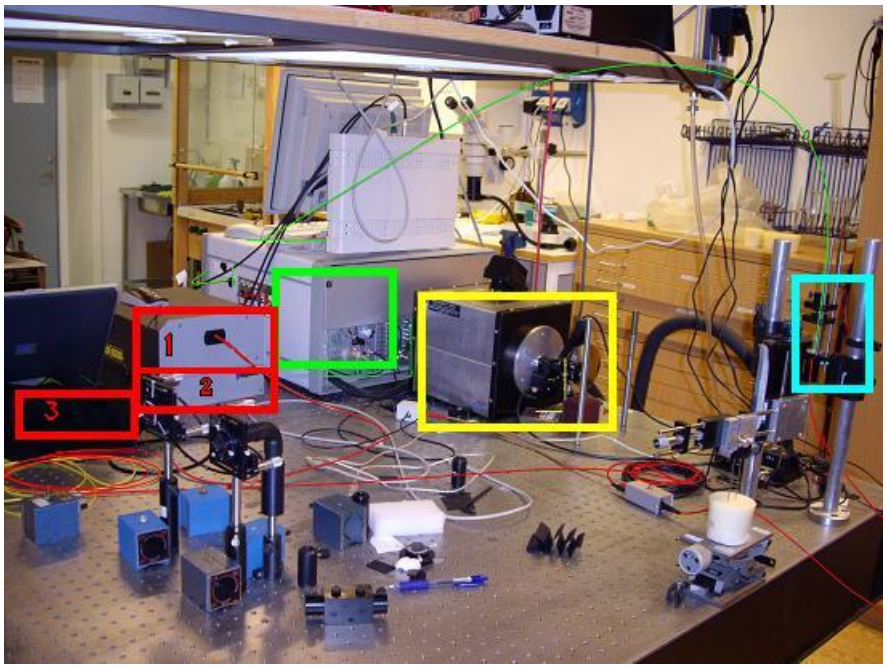

Figure 2.8: *The lab setup with the old PMT connected. The red boxes show the laser (1), the AOTF-driver (2) and the AOTF (3), and the green box the PMT (both from behind). The source fiber is marked with red and starts in the laser, and ends in the turquoise box, where the sample is to be put (now the IRF plate is placed there). The detector fibre, marked in green, leaves from the turquoise box and ends in the PMT-box. (The new PMT is marked in yellow but was not connected when the picture was taken)*

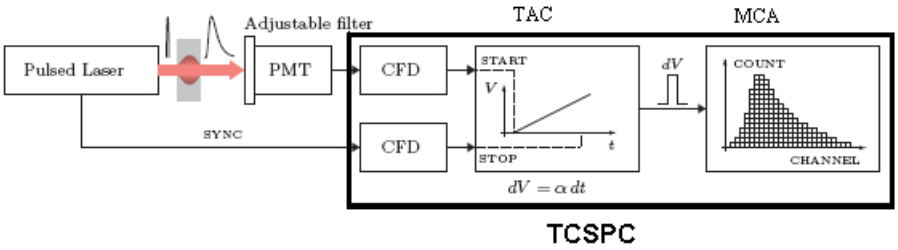

Figure 2.9: *The setup with the TCSPC-components as well as the rest of the instrumentation. [20]*

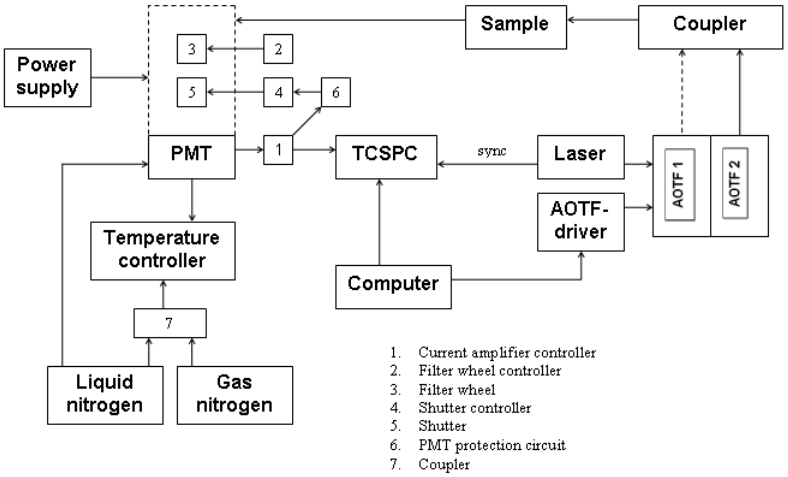

Figure 2.10: *The TOFS setup with the new PMT used for measurement the absorption and reduced scattering coefficients in the flour and grain samples.*

2.2.3 Optical Fibres

Optical fibres are used both to transport the laser light to the sample and to collect the transmitted light, bringing it to the detector.

An optical fibre consists of an inner cylinder, the core, and an outer cylinder, the cladding. Normally the core is made of a material with a higher refractive index than the cladding and the profile of the refractive index is rectangular, i.e. constant over the whole core.

Light coming into the fibre with an angle smaller than the acceptance angle, θ_a, will be totally reflected in the fibre walls and will thus be passed through the fibre. If the incoming angle is larger than θ_a, the light will pass through the fibre walls and be lost, see Figure 2.11. [22] The ability for a fibre to collect light is determined by the material it is built up of, or, more explicitly, the refractive indices of the materials, and it is called the *numerical aperture*, NA. The NA is expressed as follows: $NA = n_a sin(\theta_a) = \sqrt{n_1^2 - n_2^2}$, where

- n_a is the refractive index of air
- n_1 is the refractive index of the core
- n_2 is the refractive index of the cladding and
- θ_a is the acceptance angle of the fibre [23]

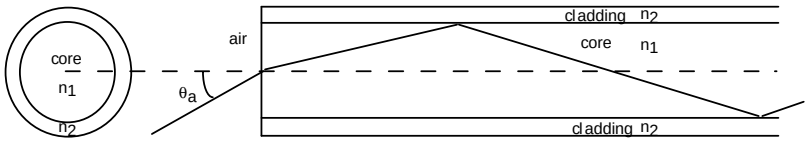

Figure 2.11: *The acceptance angel of an optical fibre is determined by the refractive indices of the fibre components, which in turn determines hte numerical aperture (NA). [24]*

The part above describes a standard optical fibre. When the light comes into this kind of fibre with different angles, it will travel with different speeds and the path lengths will be different, which means that the signal will be broadened. In the case of this setup the broadening would be much larger than the signals to be detected, and the high accuracy would disappear completely. To avoid this, *gradient index fibres* are used instead. In these fibres the refractive index is gradually reduced away from the centre. Instead of being constant over the fibre area the refractive index has a parabolic profile, see Figure 2.12. [25]

This gives the effect that a beam hitting the fibre along the centre axis will not be refracted at all; it will continue straight through. A beam hitting the fibre in a certain angle will propagate through the fibre in a sine shape, instead of bouncing back and forth as in the standard optical fibre with a rectangular refractive index profile. The optical path length of the different beams will thus not differ as much and the broadening of the pulse will be minimized.

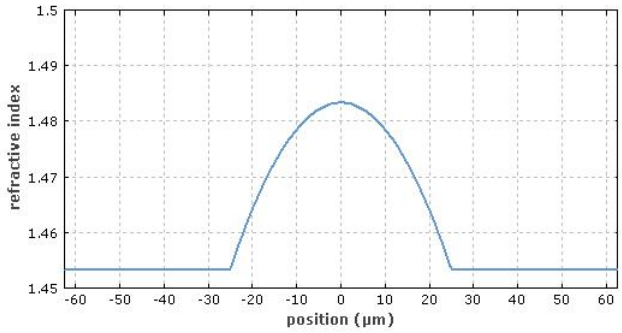

Figure 2.12: *One example of the parabolic shape of the refractive index in a graded fibre, providing the highest index in the middle of the fibre, and lower along the edge. [25]*

Chapter 3

TOFS Measurements

This chapter includes a description of the TOFS measurement procedure, the samples that were considered, and also which advantages and disadvantages that occurred for the different samples.

The measurements were made in series from 650 nm to 1050 nm with the old PMT-setup, and from 950 nm to 1400 nm with the new PMT-setup. The wavelength overlap made it possible to define possible influences of the detectors on the result. Figure 3.1 shows the absorption coefficient for dry flour without compression, measured with both the new and the old PMT in steps of 10 nm and, as can be seen in the overlap area 950-1050 nm, the generated results correspond very good to each other.

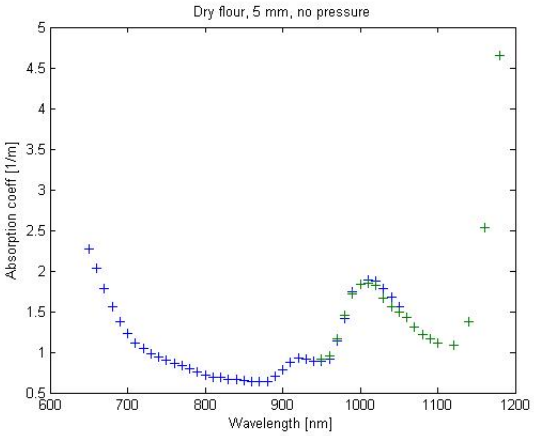

Figure 3.1: *Dry flour measured with both the old and the new PMT, the over-lapping wavelengths showing their correspondance.*

When a measurement series was made, two measurements of each wavelength were done. One with the flour sample, and one IRF-measurement (instrument response

function). The first purpose of the IRF is to compensate for all disturbances that may be caused by the system and the sample holder. The holder itself may introduce disturbances if it is constructed in a way that makes the light pass through materials other than only the sample itself. The IRF is taken by inserting a piece of black paper between the source- and detector fibres before making a measurement. The reason to use a black paper and not just air is to protect the detector from being exposed to too much light, which could destroy it.

In this case the sample holder consisted of two thin glass plates below and above the sample, and therefore they were also considered in the IRF, together with the black piece of paper.

The second purpose of the IRF is to create a point zero for the measurements to refer to. If there is a drift in the system, the IRF will catch up with it and move the zero point as well, resulting in more accurate measurements.

The outline of the measurements was to make 10 sample measurements and then 10 IRF-measurements, then switch back to the sample and so on until all wavelengths were covered. The reason of this seemingly unpractical method is to avoid possible changes in the setup to influence the results. If the sample measurement and the corresponding IRF-measurement is made close to each other, e.g. the laser will not have drifted noticeable in that short time and the result will be more accurate.

3.1 Data Collection and Evaluation

A measurement is done by collecting one data sample every second for, in this case, 20 seconds. The same procedure is performed for each wavelength. When all the required data is collected a Matlab program is used to evaluate the results. The program begins with finding the peaks in the measurements. After that it detects and removes so-called outliers, which is an incorrect measurements. It sums up the data, and finally it makes a best fit curve to the measurement points. From there it calculates a large amount of different properties, but for this work the only interesting ones were the absorption and the reduced scattering coefficients. These coefficients are then plotted with respect to the wavelength.

3.2 Flour

Before the measurements could begin a sample holder had to be designed, fitting in the existing setup. A lot of experimenting was done to come up with the best solutions for the construction of a sample holder, stable enough to ensure that the optical properties of the sample did not change during the measurements and that it was possible to make reproducible samples. The final solution became aluminium plates with holes in the middle, which were painted black in order not to reflect the light unnecessarily much. Sample holders with different depths were manufactured to make sure that the best possible signal was obtained for every sample. A hole of 5 mm depth turned out to be a good dimension for regular, dry

flour without any pressure and a depth of 20 mm for compressed flour. A cover slip made to be used in microscopy was glued to the bottom of each holder. After the flour was inserted, another cover slip was put on the top, in order not to let the fibre damage or change the surface during the measurements. The shallow sample holder is shown in Figure 3.2 and the deep in Figure 3.3.

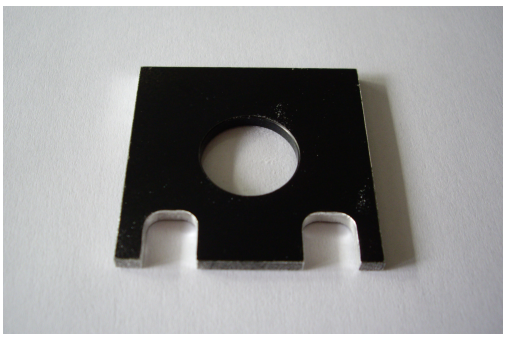

Figure 3.2: *The shallow sample holder manufactured to measure the uncompressed flour. The depth is 5 mm.*

Degree of Compaction

Flour is very easily compressed; just shaking the sample a little causes the flour to become denser. This apparent change in the structure makes it interesting to evaluate how it affects the optical properties. For this purpose the deeper sample holder, with a depth of 20 mm, was used. A cover slip was glued to the bottom surface, covering the hole. A certain amount of flour was then weighed out, with a very sensitive scale, put in the hole and another, smaller cover slip which fitted in the hole was placed on top of the flour, carefully not to compress it further. 2.0 g of flour turned out to be a fairly good amount to use for these measurements. Test measurements showed that using only 1.0 g made the flour layer very thin, and more than 2.0 g made it too thick to get a sufficient amount of light going all the way through.

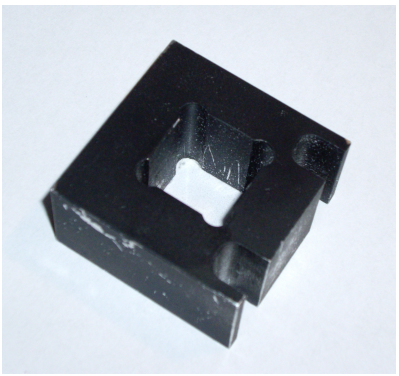

Figure 3.3: *The sample holder for the compressed flour. The depth of this is 25 mm.*

The whole sample holder was then placed on another scale and the flour was compressed to the right pressure by using a pole, fitting into the hole. The thickness of the flour layer was important for the upcoming data evaluation, and was determined with a slide calliper. After that the sample was ready to be measured. Measurements were taken every 10th nm, starting at 650 nm and ending at 1050 nm. Two pressure series were done, one ranged between 0-1000 g of pressure, with 200 g intervals. The other one ranged from 0 to 2000 g with 500 g intervals.

Samples without load were also evaluated, i.e. 0 g of pressure. These samples were prepared by putting the flour in the hole of the holder (5 mm deep) and gently scrape of all excess flour to create a flat surface, but as far as possible trying not to compress the flour. In order not to affect the surface with the optical fibre during the measurements a cover slip was placed on top as protection.

Finally the data was evaluated according to 3.1 *Data Collection and Evaluation.*

3.3 Grain

Flour turned out to be a fairly easy material to work with, even though it easily changed its structure, compared to the grains which FOSS also is working with. The grains were large, very scattering, and it was hard to find a suitable sample holder for them, which made the procedure even harder.

Different Kinds of Grain

Two kinds of grains were evaluated in this project; wheat and barley. The optical properties for those two were expected to differ quite a bit. Different kinds of flour are rather similar and there were other factors, such as the compression, which influenced the result considerably more. In the case with the grains the difference between themselves was supposed to be more noticeable.

The grain measurements were made partly in an existing sample holder from FOSS, shown in Figure 3.4, and also in the deeper flour holder. The holder shown in the picture is the same kind used in the instrument Infratec™ Sofia, which was used to obtain reference data for the grains. The first difficulty with this holder was that it was not constructed to fit in the TOFS setup, which brought the problem that the fibres did not end up in the middle of the holder, but rather close to the edge. This could of course lead to unwanted side effects, but it was not possible to change the setup in a way that made it fit better.

Another thing differing between the flour- and the grain measurements were the IRF. It was stated earlier that the IRF- and sample measurements were made 10 of each and then switching, in order not to let the system drift. This was hard to accomplish with the grains, since it was impossible to put the sample back in the exact same position as before. Even the slightest rotation of the holder caused big differences in the result, and by removing it completely several times would make the result useless. Instead, all sample measurements were done first, then all the IRFs. In case of some drift in the system, this would not be noticeable in comparison with the disturbances caused by moving the sample.

Figure 3.4: *Sample holder made for analysing grain in the FOSS instrument Infratec™ Sofia.*

"Strange" barley

A "strange" sample of barley was discovered at FOSS; measurements in two different instruments resulted in completely different data, compared with their normal samples. In an attempt to elucidate the reason to the behaviour of this sample it was decided to perform TOFS measurements on it. These measurements and the following data evaluation were carried out in the same manner as those for the other whole grains.

Chapter 4

Simulations of FOSS Instruments

One important task in this work was to set up models of different instruments manufactured by FOSS. The parameters obtained with time-of-flight spectroscopy measurements were used to simulate the instrument response for deviating samples, i.e. with deviating optical parameters. This would give FOSS the opportunity to simulate possible changes in their constructions instead of modifying the instruments and perform large numbers of test measurements.

4.1 Flour

Besides the optical properties, the transmission of light through a powder also depends on the size and shape of the grains and the size of the cavities between the grains, as well as conceivable contamination particles, e.g. water molecules. The larger the particles in the powder are, the less light will be transmitted. [26, 27]

It has been shown that flour has similar optical properties as other powders, such as sugar or salt, and, when compressed into a sample holder, the properties are also similar to those of pharmaceutical tablets, previously examined with TOFS. As described earlier in section 2.1 *Light propagation in flour and grain*, two alternative ways to describe the scattering caused by small particles exists; either by Mie theory, for spherical particles of the same size as the wavelength, or by Rayleigh theory, for particles much smaller than the wavelength.

In earlier studies of different granular solids, among them flour, it has been shown that the average grain size was 150-200 μm and that the particles were fairly spherical, which means that Mie theory is valid when investigating flour. [27] Since this number was compiled from regular flour, it is assumed to be valid for the regular flour used in this case too.

It has also been shown that the diffusion theory is valid for scattering materials as e.g. pharmaceutical tablets, and, more importantly in this case, it may be assumed valid also for flour. [13]

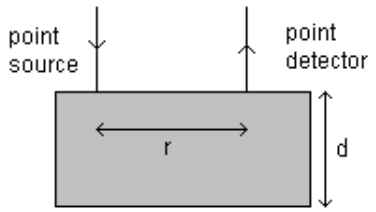

(a) *Point source and point detector*

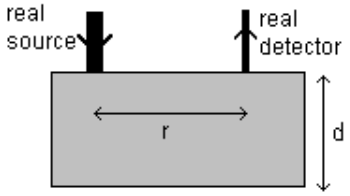

(b) *Source and detector with real extensions*

Figure 4.1: *Schematic figure of the simulation model*

The simulations were carried out in Matlab and the starting point were the diffusion theory applied to a geometry consisting of a thin slab. An optical fibre, modelled as a point source in $(r, z) = (0, 0)$, induces the light into the slab. Then the reflected light that reaches the detector, located a vertical distance r from the source, were to be calculated. See Figure 4.1a.

This was performed by using the equation for spatially resolved reflectance derived in 2.1.6 *The Diffusion Equation*, and shown in its entirety in Appendix A.

This formula uses a point source and a point detector, but the real instruments have both a source and a detector/detectors with certain extensions, shown in Figure 4.1b. It was thus necessary to extend those to the right dimensions. This was done by integrating the light intensity over both the source and the detector areas. The particular instrument used to measure the flour has 6 detectors spread out around the sample. Three of them cover the wavelengths up to 1050 nm, which is the range used in this project, the three other cover the rest of the spectra, up to 2500 nm. This was modelled as one large detector, since all light was to be detected somewhere, and it was not important in which detector each photon ended up.

It is also probable that the source does not emit the light equally distributed over the whole opening area. To compensate for this, the input was supposed to follow a Gaussian distribution. The same argument was supposed to be valid for the detector.

The path lengths between the different parts of the source and the parts of the detector are not equal, since both source and detector has certain extensions. Also, because the deeper the photons go into the medium, the longer the path length becomes, see Figure 4.2. This problem was taken care of by calculating the contribution from every element of the source in every element of the detector, and sum up the result for all detector elements. The last part to consider is the numerical aperture of the detector, introduced in 2.2.3 *Optical Fibres*. The output was finally recalculated from reflected light reaching the detector, to the absorbance in the sample, since this is the output from the instrument used at FOSS.

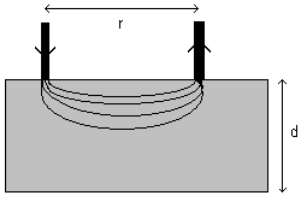

Figure 4.2: *The deeper laying paths are longer than those more shallow.*

The proportions of the used instrument, are shown in Figure 4.3.

By using values of the input parameters corresponding to those of e.g. different kinds of flour or compressed samples, it should be possible to predict the response from a FOSS instrument, without actually making a measurement on a real sample. The big advantage for FOSS would be that they do not have to modify their instruments to able to see what changes in output a thicker/thinner sample or a transversally moved sample would result in.

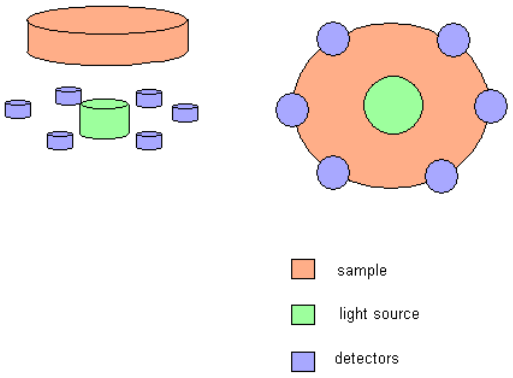

Figure 4.3: *Sketch of the instrument used to measure the flour. Left: Seen from the side.Right: Seen from beneath.*

4.2 Grain

A big difference between grains compared with flour is the size of the granules. It results in important differences in the optical parameters, and also in which modelling methods that should be used. The grains are not spherical, and can not be approximated as spherical. See Figure 4.4. Thus the light scattering can not be approximated with Mie theory. [27] Rayleigh theory is of course not valid either, since the granules are obviously much larger than the wavelengths. The diffusion equation is however still used since no better options are available.

The bigger the grains, the lower the transmission gets. Since these granules are many, many times bigger than the flour particles, the transmission is also many

Figure 4.4: *The grains are not spherical. Barley to the left and wheat to the right.*

times lower. Higher transmission is obtained if the grains are compressed, since the air cavities in between them will shrink. [26]

The spatially resolved version of the transmission equation, derived in 2.1.6 *The Diffusion Equation*, and shown in its entirety in Appendix A, was used. Like the equation used for the flour calculations, this only gives the transmittance from a point source, transmitted into another point; the detector. Thus the same procedure as carried out for the flour is needed in this case too, in order to compensate for the extension of both the source and the detector. The other corrections made in the flour simulation; different path lengths, Gaussian weight functions and numerical aperture, had of course to be made for the grain simulations as well, and in the end the transmitted light is transformed into absorbance since this is what the FOSS instrument measures. In Figure 4.5 the model is shown.

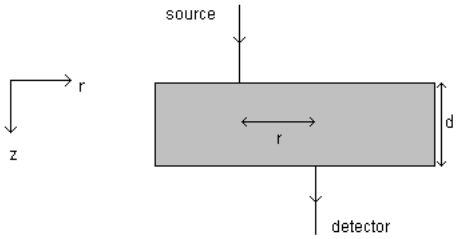

Figure 4.5: *Transmission mode setup for the simulations.*

The proportions of the instrument used to measure on grain are shown in Figure 4.6.[1] The light beam from the lamp is approximately 30 mm in diameter at the sample surface. The detector fibre consists in reality of a bundle of 30 fibres, each with a diameter of 110 µm, and together they can be approximated as one, with a diameter of 700 µm. The numerical aperture of this fibre is 0.22.

4.3 Correction algorithms

As mentioned in the previous sections the procedure was to measure flour and grains with TOFS, to obtain the scattering and absorption coefficients for different wavelengths. Afterwards, using the coefficients in simulations of FOSS

[1] Picture drawn by Christoffer Abrahamsson, FOSS

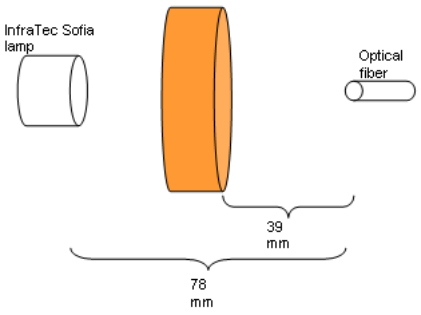

Figure 4.6: *Geometry and proportions of the grain instrument used in the simulations.*

instruments, and in the end hopefully get a result that was in accordance with measurements made with the instruments from FOSS. This result was thus not obtained only by the simulations. Since the samples in question are highly scattering, this will affect the result to a great extent. Of course FOSS already knows about this problem, and they have developed algorithms to compensate for the scattering. The same algorithms have been used for the simulation data, and the goal of this section was to obtain data that corresponds to the real, measured control data. In that way it would be possible to predict how a deviating sample will behave.

4.3.1 Standard Normal Variate

The degree of the scattering is dependent on various factors, such as the wavelength, the particle size and the refractive index, which result in different scattering effects throughout the spectra. Two effects can be seen; *multiplicative* and *additive* effects. The multiplicative ones appear as every value in the spectra has been multiplied by a constant, and the additive as a constant has been added to every value. These effects show as tiltings and shiftings in the spectra. To compensate for them Standard Normal Variate Transformation (SNV) may be used.

The method amounts to first centre each spectra by subtracting the mean value of the spectrum, $\bar{A}$, from the spectrum itself, and then scaling it with the standard deviation of the sample spectrum, σ:

$$A_{i,SNV} = \frac{A_i - \bar{A}}{\sigma_A}$$

After applying this method, the mean value of the spectra is 0 and the variance is 1. SNV primarily reduces the multiplicative effects. [28, 29]

4.3.2 Multiplicative Scatter Correction

The main differences between Multiplicative Scatter Correction (MSC) and SNV are that MSC is more complicated and that the spectrum is not centred after the treatment. The procedure begins by plotting all spectra in the scan against the scan's total average spectrum. This would give rise to straight lines, beginning in the origin and with a slope equal to one, if there were no multiplicative or additive effects. With those effects present the lines will have an offset, $O(n)$, and a certain slope, $S(n)$, separated from one. Each spectrum is subtracted by the corresponding offset, and divided by the corresponding slope to correct for the effects caused by the scattering:

$$A_{i,MSC}(n) = \frac{A_i(n) - O(n)}{S(n)}$$

Chapter 5

Measurements with FOSS-instruments

To have something to aim at for the simulations discussed in the previous chapter, measurements were also made with FOSS instruments, to obtain reference data. The instruments used are briefly presented in this chapter.

5.1 XDS Biodiesel Analyser™

The XDS Biodiesel Analyser™, shown in Figure 5.1, is developed to analyse samples from every step in the production of biodiesel, from the crude oil, and in-process samples, to the finished product. It can also analyse other samples, as long as they can be placed in the sample holder. The instrument illuminates the sample from below with a halogen lamp, generating a spectrum from 400 to 2500 nm. By means of a scanning monochromator the different wavelengths are separated from the white light. Six detectors are placed around the sample to detect the reflected light. Three of them are made of silicon and they are used in the spectral region up to 1050 nm, which is the range of the measurements in this project.

Compared to the measurements made with the time-of-flight setup, it was considerably more convenient to measure with the XDS-system. The sample was placed inside the machine, above the light source and the detectors, and two measurements were made; one empty as reference and one with the sample inserted. The produced data was transferred into Matlab where a graph could be plotted.

The same measurement series performed with time-of-flight were done with the XDS, i.e. changing the pressure of the sample from 0 g to 2000 g, with 500 g intervals. Three measurements for each pressure were done, to make sure that everything was reproducible. (Even tough this probably is already well examined by FOSS)

5.2 Infratec™ Sofia

To analyse the whole wheat and barley grains the FOSS instrument Infratec™ Sofia, shown in Figure 5.2 was used.

The main purpose with the Infratec™ Sofia is to give the agriculturists a chance to know exactly when to start harvesting their crops, by bringing the instrument with them out to the field and taking samples. In that way they can harvest different areas when optimal conditions are achieved, and thus get optimal payment for their products.

Infratec™ Sofia is a transmission instrument using a halogen lamp to illuminate the sample, and a DDA (Diod Array) spectrometer made of silicon as detector. Since the instrument is supposed to be carried around in a field there are no moving parts, e.g. no scanning monochromator, in it. Instead the white light from the source hits the sample, and on the other side of the sample it hits a lattice which separates the different wavelengths so that they each hit one certain part of the detector array.

The Infratec™ Sofia has a wavelength span of 850-1050 nm, and it is built to measure different types of grain, as well as flour. Some examples are barley, corn, rice and wheat, among many other types of grains. It evaluates the protein and moisture content, which are important nutrition and storage factors. For wheat it can also give the amount of gluten, which determines how good dough the wheat flour will give rise to. [30]

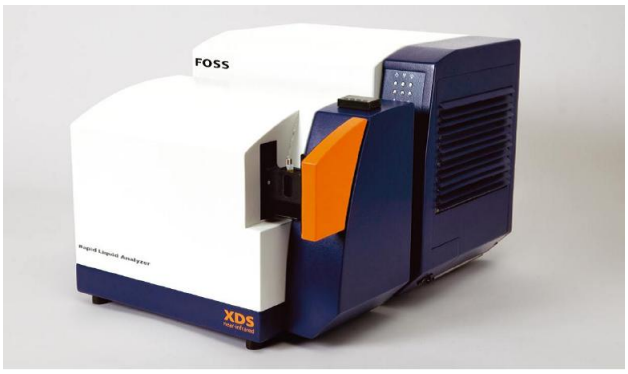

Figure 5.1: *The XDS Biodiesel Analyser™ used to measure the flour samples. [31]*

Figure 5.2: *The instruments used to measure the whole barley and wheat grains; Infratec™ Sofia. [30]*

Chapter 6

Results

6.1 Flour

6.1.1 Time-of-Flight

The first step to be taken was to attain reproducible samples. This turned out to be a bit of a problem since flour easily changes its structure and degree of compaction with the smallest exterior force. This problem appeared mainly with the totally uncompressed samples. The compressed samples turned out to be easier to make reproducible. At first samples compressed by pressures ranging from 0 to 1000 g with 200 g intervals were measured. The variation of the absorption coefficient was as good as the same for all the samples, as expected. The scattering coefficient was supposed to grow when the pressure was increased. This was confirmed by the time-of-flight spectroscopy measurements. It was also discovered that the differences between the different compressions were not very big, and the results became very similar to each other. Sometimes a lower pressure also got a higher scattering coefficient than the higher pressure.

If a large amount of measurements for each pressure would have been made, confidence intervals could have been constructed. This would probably have shown that the intervals for the scattering coefficients for different pressures partially overlap, but it would have shown that increased pressure is followed by increased scattering. It was not considered necessary to perform all these measurements as it would have taken a lot of time, and would not contribute enough to the final result. Instead the conclusion was drawn that the pressure intervals were too small, and therefore measurements with higher pressures and bigger intervals were made.

With pressures ranging from 0 to 2000 g, with 500 g intervals the result got more satisfying. In this case only the top pressures, 1500 and 2000 g, interfered with each other. Otherwise the reduced scattering coefficient was clearly increasing with the increasing pressures. Figure 6.1 shows the scattering coefficient for a

pressure series with 500 g intervals and Figure 6.2 shows the absorption coefficient for the same pressures.

After having compared with more measurements performed under the same conditions the conclusion was drawn that both the measurement method and the sample preparation was good enough to yield reproducible results, and that the results shown in Figure 6.1 and 6.2 were to be used in the simulations of the instrument from FOSS.

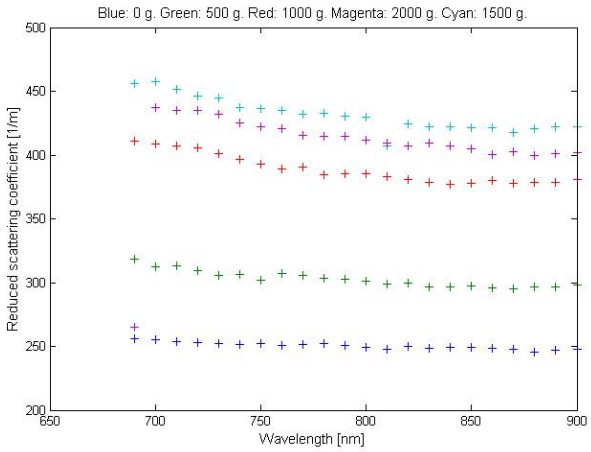

Figure 6.1: *Comparison of the reduced scattering coefficient measured with the TOFS system between flour samples with different pressures. Pressures ranging from 0 g to 2000 g.*

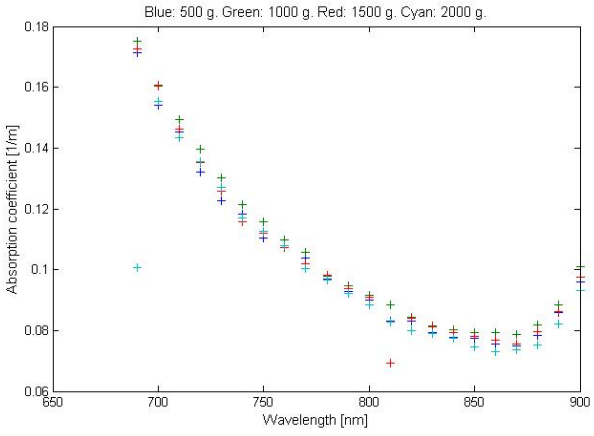

Figure 6.2: *Comparison of the absorption coefficient measured with the TOFS system between flour samples with different pressures. Pressures ranging from 0 g to 2000 g.*

6.1.2 XDS Biodiesel Analyser™

The measurements with the XDS Biodiesel Analyser resulted, as before, in different curves for the different pressures. Those are shown in Figure 6.3. Since the output from the XDS, unlike the time-of-flight result, is absorbance, the scattering is scaled away. It is still possible to see some variation between the different pressures, but it is extremely small. The biggest difference was estimated to appear around 800 nm, between 0 g (red) and 500 g (green) and was calculated to be 0.00512 absorbance units. The conclusion was thus that the result is as similar as possibly attainable for the different pressures, and that it was this result that the simulations should reproduce.

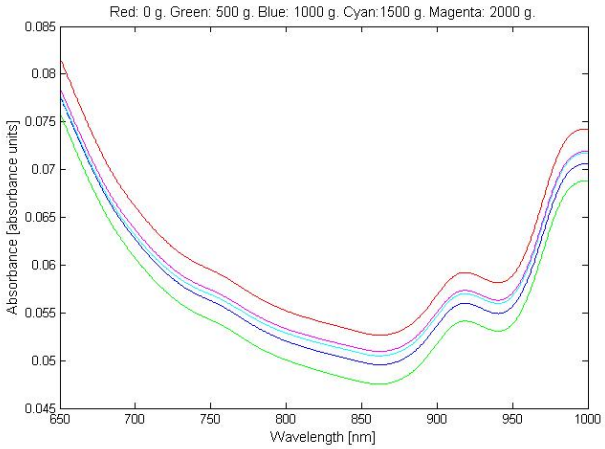

Figure 6.3: *The absorbance as a function of wavelength for samples with different pressures, produced with the XDS at FOSS.*

6.1.3 Simulations

The aim of the reflection simulations was to reproduce the same spectra as was generated with the XDS instrument. The first problem that came up was to assign values to some constants. To be able to choose as good constant values as possible it was decided to try to reproduce an uncompressed sample. This simulation would then be used for the compressed samples as well, with the same constants.

By using only the diffusion equation the desired result is not achieved, since the output becomes reflectance/transmission, and the reference data is absorbance. By using the diffusion equation the scattering will affect the result, and since the scattering differs from sample to sample, the final result will also differ. Therefore it was necessary to apply some kind of correction to compensate for the scattering. As was written in 4.3 *Correction Algorithms*, FOSS uses two methods; SNV and MSC, and it was their code that was used in this project. Since both methods are based on similar theories, only one of them is used at a time. Just to get a full picture and to be able to compare they were used together on this data as well.

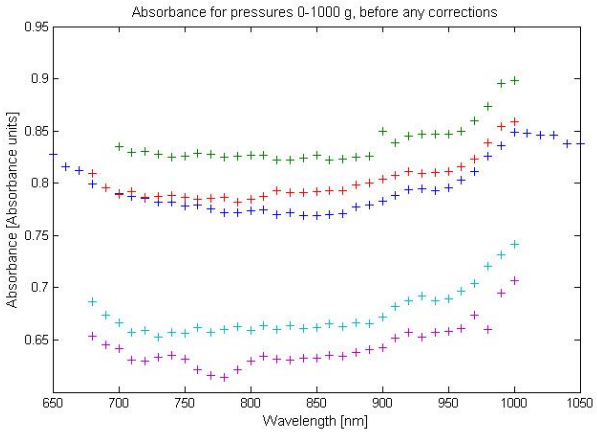

Figure 6.4: *Absorbance for different pressures without correction for the scattering.*

Figure 6.4 shows the absorbance for different pressures before any corrections are made, Figure 6.5 shows the absorbance after both SNV and MSC correction.

By comparing the simulated results with the XDS result the overall structure of the curves are pretty much alike. The XDS measurement uses more wavelengths; every 0.5 nanometre instead of every 10 nanometre, as was the case with the TOFS measurements. That, and some curve fitting, makes the XDS-graph a lot smoother than the simulated result.

For comparison purpose a polynomial was fitted to the simulated and scattering corrected values of the uncompressed sample. Three different curves were fitted, one to the result corrected with SNV, one to the MSC-corrected, and at last one to the result corrected with both methods. The correspondence between these curves and the XDS-curve turned out to be fairly good. By comparing the two graphs in Figure 6.6 with the XDS-result in Figure 6.3, one can see that the overall patterns are very alike. The same bumps are there, although there are some small differences in the absolute numbers. Both simulated results agree with the real measurement at the minimum value; they all reach approximately 0.055 a.u. at around 850 nm. The maximum peaks are more different, the real measurement has its highest value in the beginning, at 650 nm, whereas the two simulated results have their maxima in the end of the spectra, at 1000 nm. Hence the peak at 1000 nm differs: 0.07524 a.u. for the real, 0.08773 a.u. for the SNV-corrected and 0.09995 a.u. for the MCS-corrected. This turns out to be a deviation of 14.2% and 24.7 % respectively, which must be considered as quite a lot. But, this is where the correspondence is as worst. By instead looking at the minima at 850 nm the values are 0.05268 a.u. in the real measurement, 0.05429 a.u. for the SNV-corrected and 0.05386 a.u. in the MSC-corrected. This instead gives deviations of 3.0% and 2.2%, which must be considered as a very good correspondence, since the deviation between the different curves in the XDS-measurement is 9.7% at 850 nm. The large deviation at 1000 nm (and the smaller at 650 nm) is probably a consequence of the values of the constants mentioned earlier.

Finally curves were fitted to the compressed samples too. This was done in order to evaluate how exact the simulation became, by using the constants determined in

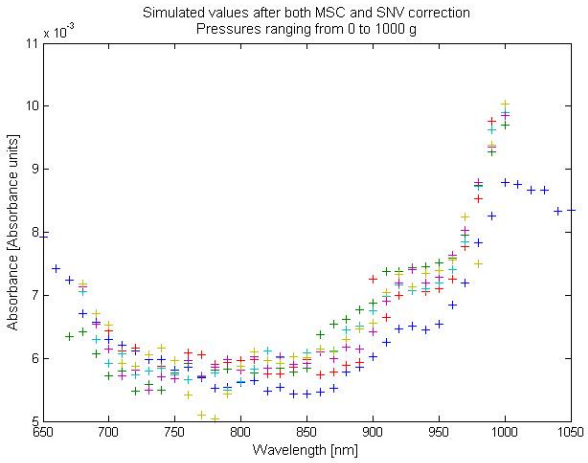

Figure 6.5: *Simulated absorbance values for pressures 0-1000 g after both MSC and SNV correction algorithms has been applied.*

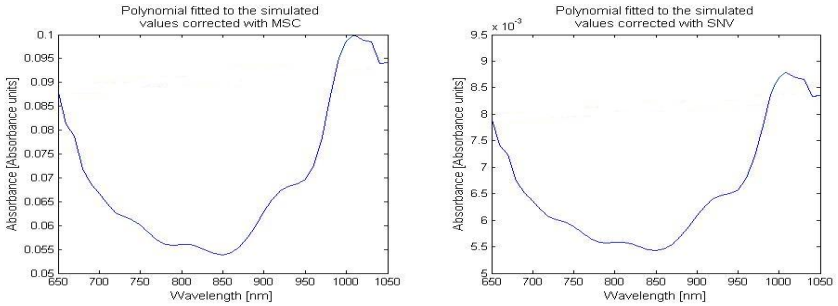

Figure 6.6: *Polynomials fitted to the simulated values corrected with MSC (to the left) and SNV (to the right)*

the zero-pressure case. The curves are shown in Figure 6.8. The first observation is that the fitted curves are not as regular as the measured ones, nor are they as evenly spread out. Instead the simulated curves cross each other; they go up and down and follow the same pattern as neither the real curves, nor the simulated 0-gram pressure curve. Some explanation to this behaviour is of course the measurement procedure, where the sample was moved several times during one measurement and the influence of the fibre, which, in spite of the protecting cover glass, possibly could have changed the surface of the sample enough to make an imprint in the final result.

Disregarding the obvious differences, the result is not too bad. As written previously in this section the biggest absolute difference between two of the curves in the XDS result was 0.00512 a.u. at 800 nm. The simulated result shows a difference of 0.000427 a.u. at 800 nm, which thus is even better.

The biggest difference in the simulated result occurs at 920 nm, where the span is 0.00103 a.u. and the corresponding XDS value is 0.00509 a.u. It seems that

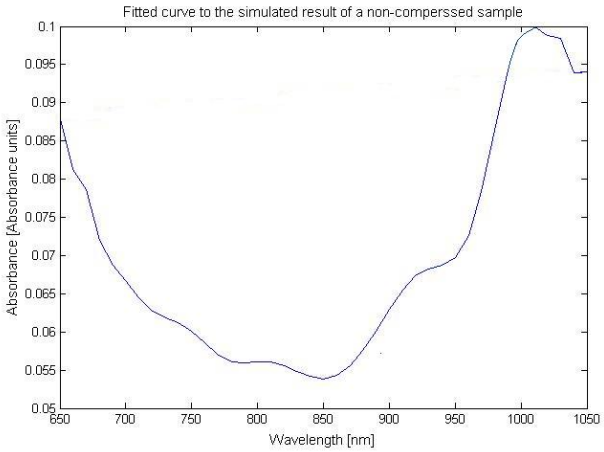

Figure 6.7: *A fitted curve to the simulated result of a non-compressed sample. The simulated result is corrected with both SNV and MSC.*

the simulated result is better than the XDS, if one only consider the absolute values. The shapes of the curves are not as good, and they do not follow the same patterns as well as the XDS result. Another difference between the two results is that the XDS reaches its highest values around 650 nm, and the maximum at 1000 nm is considerably lower. The simulated result gives the opposite, highest values at the peak at 1000 nm, and lower values in the beginning of the spectra.

Despite those differences the simulated result must nevertheless be considered to be satisfactory, even though not yet good enough to be used.

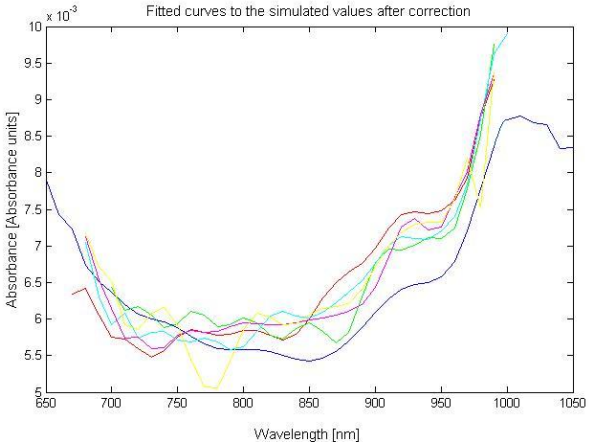

Figure 6.8: *The fitted curves to the simulation of pressures between 0 and 1000 g.*

6.2 Grain

6.2.1 Time-of-Flight

It was generally harder to perform the measurements on the grains, than the flour. The samples were much more sensitive to movements since the grains were bigger, which means that a small rotation of the sample resulted in a completely new structure. Compared to the flour samples these results did not become as good. The absorption coefficient that were very stable for the flour varied a lot for both barley and wheat, but the overall shape was the same. The reduced scattering coefficient was tricky to measure for the flour, and became even harder for the whole grains. After several measurements it was possible to get results that looked similar to each other, but many measurements ended up to just noise, with no distinguishable pattern at all.

During the measurements it was discovered that the sample holder from FOSS (Figure 3.4) was usable for the wheat, but with the barley grains, the light could not pass through the 0.02 m thick sample. Instead the deeper flour holder (Figure 3.3) was used to obtain samples of varying depths. 0.01 m turned out to be a fairly good thickness of these samples. Some measurements were made with wheat in this home-made holder too, and these results turned in fact out to be better than those obtained with the deeper FOSS-holder.

The biggest reason to the large variations in the results is probably that the structure of the samples became very different every time the grains were put in the holders, and this affected the results to a very large extent. The result for the wheat is a little better, which probably is due to the fact that the shape of those grains made the sample more compact, there was not as much air in between them as it was in the barley sample.

Barley

Figure 6.9 shows the absorption coefficient for three barley samples. Generally they follow similar patterns, but it was definitely harder to obtain this degree of reproducibility than it was with flour. The values are in the same range for all three samples, but they do clearly not follow each other as well as the absorption coefficient for the flour did. But after all, a minimum at around 900 nm, and a peak at 1000 nm, representing the amount of protein, are distinguishable in all versions of the spectra.

The reduced scattering coefficient was even harder to get good values for. Many times the output was only unusable noise. But after several attempts some fairly good results came up. Figure 6.10 shows three graphs of the reduced scattering coefficient, the lower one really smooth, but the similarities between this one and the other two are unfortunately not many, not the position of the peak, nor the range of the absorbance values.

A “strange” barley sample was also evaluated, one that gave different results in all versions of FOSS’s grain instruments. The expectation was that the time-of-flight measurements would bring some light to the strange results. The absorption

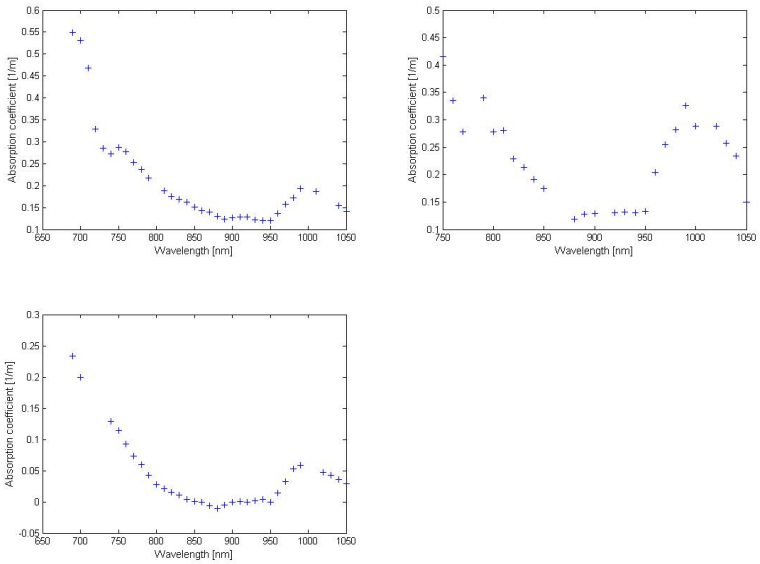

Figure 6.9: *The absorption coefficient for three barley samples. They have almost the same shape, but compared to each other they are displaced by a constant factor.*

and reduced scattering coefficients for this sample are shown in Figure 6.11 and 6.12 respectively. By studying the graphs with the absorption coefficient and comparing them with the ones showing the coefficient of the "normal" barley samples, unfortunately no clear difference stands out. Graph number three in both sets are the most similar according to shape, and the only difference between them are that the peak is situated at around 940 nm, compared to around 890 nm, for "normal" and "strange" barley respectively. This is not a huge difference and probably not enough to say anything about the reason to the strange behaviour, especially since the differences between the samples of the same kind are so large. The peak mentioned moves a little back and forth from sample to sample, making it an unreliable source of error. The absorption coefficient for both the normal and the "strange" barley vary just as much between each other as they do within the same group of sample, so nothing is revealed there either.

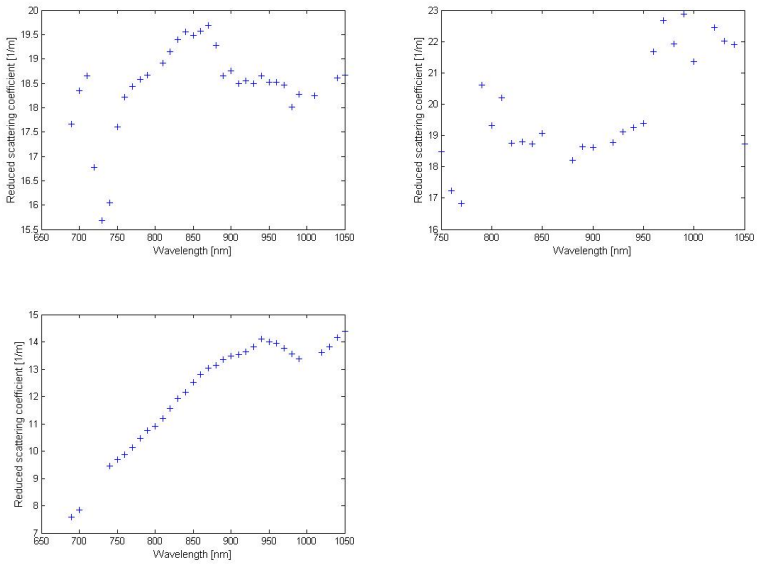

Figure 6.10: *Reduced scattering coefficient for barley three barley samples. One of them has a really nice shape, but in the others one can only divine that shape.*

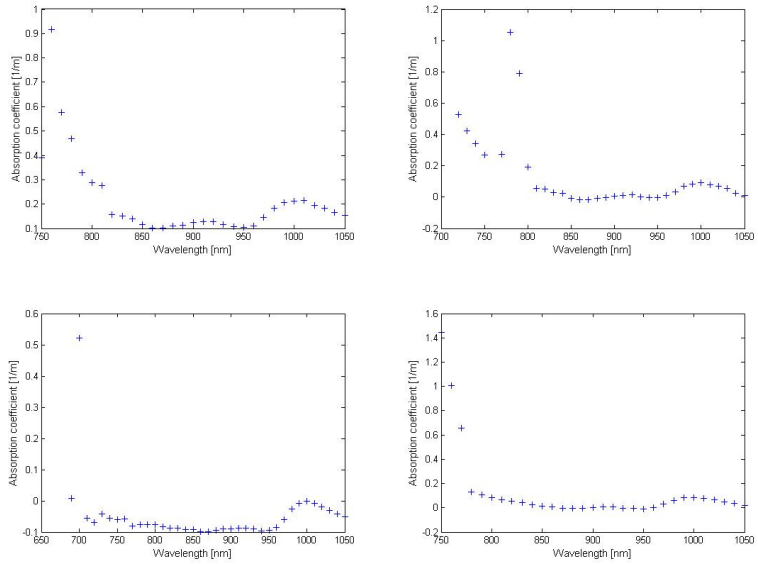

Figure 6.11: *Absorption coefficient for four measurements of the strange barley.*

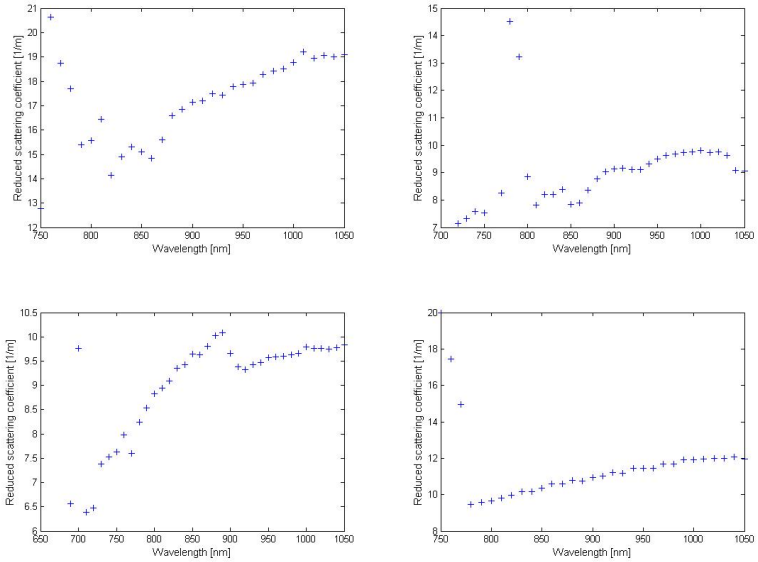

Figure 6.12: *Reduced scattering coefficient of the strange barley sample.*

Wheat

The absorption coefficient for wheat was not very reproducible either, to some amount the shape of the curve is similar, but still not nearly as good as the result of the flour. The absorption coefficients for some of the evaluated wheat samples are shown in Figure 6.13.

The reduced scattering coefficient on the other hand was really hard to measure accurately. In fact only one measurement resulted in presentable data, which is shown in Figure 6.14. The curve is very uneven and makes a large jump around 750 nm, which probably is due to some kind of error in the measurements. Still, it is possible to see a pattern. The other measurements only resulted in a useless, constant noise.

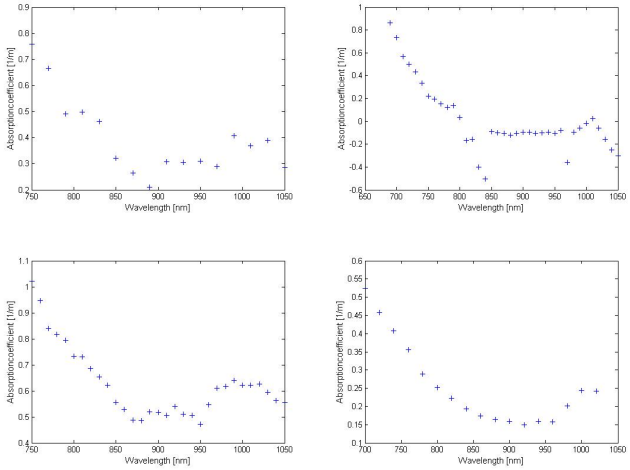

Figure 6.13: *Absorption coefficient for four wheat samples.*

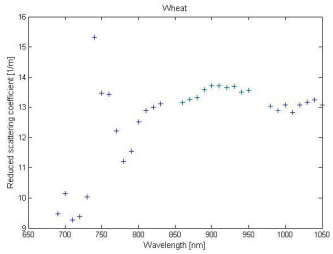

Figure 6.14: *Scattering coefficient in wheat.*

6.2.2 Infratec™ Sofia

Reference measurements were made for all three kinds of grain samples; barley, strange barley and wheat, with the transmission instrument Infratec™ Sofia. The output of this instrument was absorbance, and the results are shown in Figure 6.15. It was these graphs that worked as the models which were to be strived to imitate with the simulations.

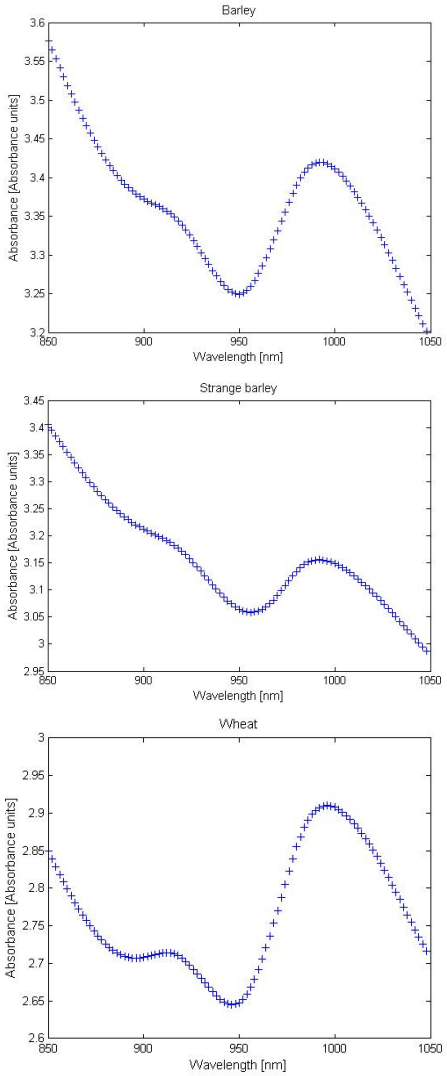

Figure 6.15: *Absorbance spectra for, from top to bottom, a normal barley sample, a strange barley sample, and wheat.*

6.2.3 Simulations

As for the flour the aim was to reproduce the same result with simulations as achieved by measurements with Infratec™ Sofia. Since the TOFS-results for the grain samples did not turn out to be particularly good, the expectations were not very high for the simulations, as those were based on the spectroscopy result.

Barley

The expectations were low, and the worst case scenario was that the simulations would not give anything at all, but that fortunately turned out to be wrong. Figure 6.16 shows the whole spectra of the simulated result, and Figure 6.17 a close-up of the important area. These two graphs are to be compared with the graph of barley in Figure 6.15.

Both differences and similarities can be found in the two simulated graphs, Figure 6.16 and 6.17, compared with the one made with the Infratec™ Sofia, Figure 6.15. One similarity is the peak at 1000 nm, which clearly stands out in the simulations as well. The peak reaches 3.43 a.u. in the measured result, compared to 3.52 and 3.44 a.u. respectively for the simulations. This is about as far as the similarities go. There is indeed a dip at 950 nm in all graphs, but the values start to differ considerably more now; 3.25 a.u. in the measurement, compared with 3.33 a.u. and almost 3.38 a.u. Continuing to the plateau at 900 nm, it has transformed into a peak in the simulations, but the values agree very well; 3.37 a.u. compared with 3.35 and slightly above 3.38 a.u. The Infratec™ Sofia-data begins at 850 nm, with 3.57 a.u. At this point the largest divergence appears; the simulations reach only 3.33 and 3.38 a.u. The real result reveals a much steeper slope than the simulated result. To sum up the result of the barley simulations it is clear that the deviations are large, and only in some specific points do the measured values agree with the simulated, and not even the shapes of the curves are particularly similar.

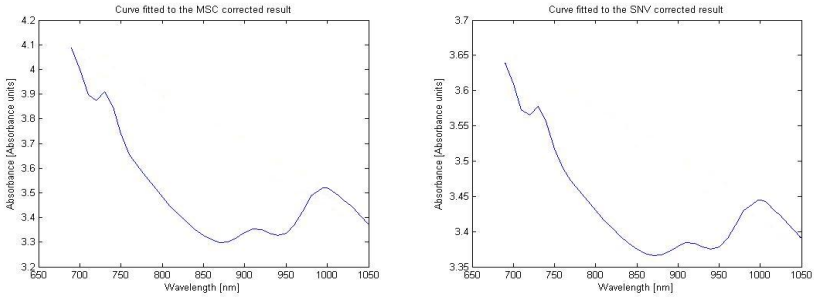

Figure 6.16: *Simulated absorbance curve for whole barley grains, corrected with SNV to the left, and corrected with MSC to the right.*

The strange barley sample showed large differences compared with the normal sample when evaluated with the Infratec™ Sofia instrument. The question was

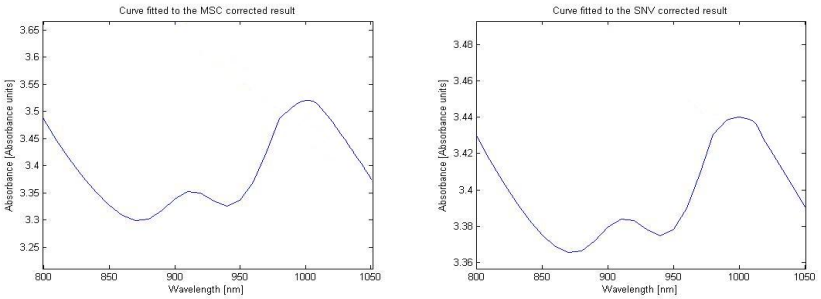

Figure 6.17: *Close-up of the simulated absorbance curves for barley, cut out to makes the comparison with the real result easier.*

then if those differences could be explained by the time-of-flight measurements and the simulations?

By beginning with evaluating the agreement between the simulated and real results, some resemblance with the normal sample appears. As with the normal sample, the real result shows one plateau and one peak, whereas the simulation results in two clear peaks. The plateau in the real measurement of the strange sample lays at 3.2 a.u. while the first peak in the simulations only reach 3.15 and 3.07 a.u. Continuing with the second peak, at 1000 nm, the real result is 3.15 a.u., compared with the simulated 3.23 and 3.12 a.u. The dip between the peaks lands in reality on 3.05, where the simulations give 3.09 and 3.04, which is the best correspondence obtained in this case. As before, the slope beginning at 850 nm is a lot steeper in the real result than in the simulations, and lead to a very bad correspondence in that area. The simulations do correspond moderately to reality, but the uncertainties and deviations from the real result make it impossible to say anything about what properties that separate the normal sample from the strange one.

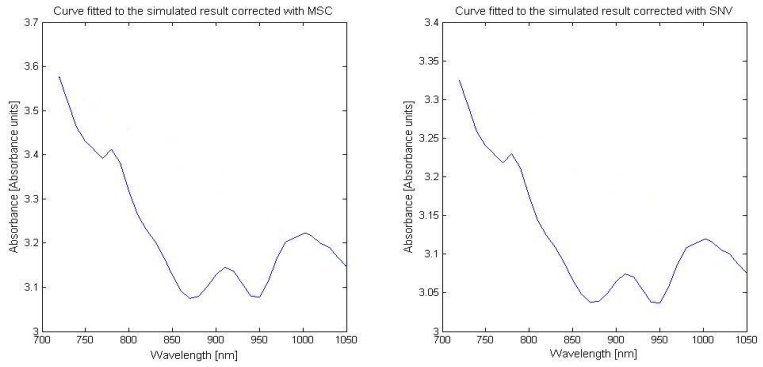

Figure 6.18: *The strange barley sample gave a result that partially differed compared with the normal barley, but it also showed many similarities.*

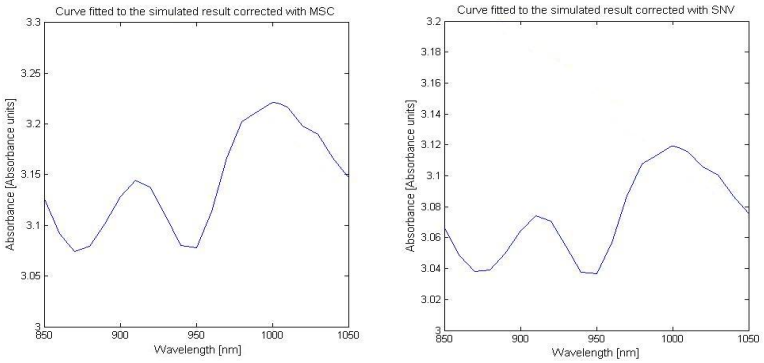

Figure 6.19: *Close-up of the result of the strange barley sample.*

Wheat

The reduced scattering coefficient for wheat was, as mentioned earlier, very hard to measure with time-of-flight spectroscopy, and as the simulations were based on bad result, the expectations were, just as for the barley, low. But since the simulations intend to remove the effects caused by the scattering, the final result was not bad at all.

The whole graph is presented in Figure 6.20, and a close-up in Figure 6.21. The close-up clearly shows that the shape of the real curve compared with the simulated agree, and by taking a closer look, it is quickly revealed that also the values are good. The four main points; the two peaks, the dip between them, and the first measurement point, at 850 nm, reach quite similar values for both the real and the simulated results.

The first peak (or at least almost a peak in the measured result) at 910 nm, reaches 2.71 a.u, compared with the simulated 2.65 and 2.71 a.u. The second peak at 1000 nm has a value of 2.91 a.u., where the simulations show 2.94 and 2.89 a.u. respectively. The dip at 940 nm goes down to 2.65 a.u. in reality, 2.62 and 2.69 a.u. with the simulations. The last point, at 850 nm, the real value is 2.85 a.u., and the simulations show 2.69 and 2.73, which again shows that the simulated slope does not increase fast enough. Despite the bad time-of-flight result, the simulated result did not turn out that bad after all. Still it is far from perfect, especially in the edges, but surely better than the expectations.

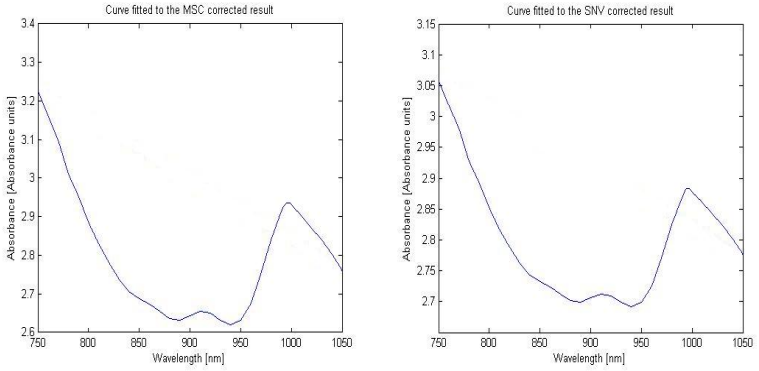

Figure 6.20: *Curves fitted to the simulated results for wheat, the left graph has been scattering corrected with MSC and the right one with SNV.*

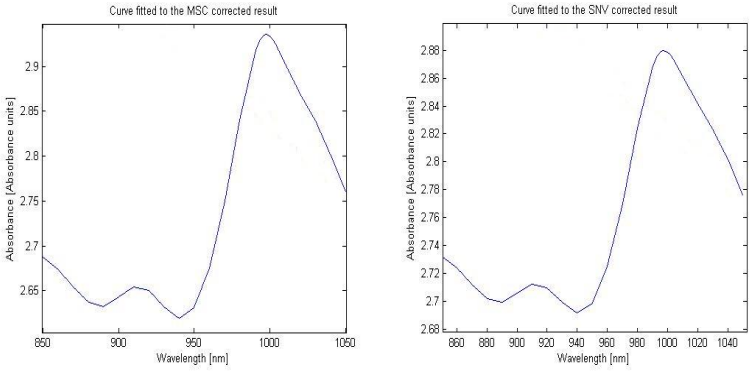

Figure 6.21: *Close-up of the simulated absorbance curves for wheat, cut out to makes the comparison with the real result easier.*

Chapter 7

Conclusions and discussion

The time-of-flight measurements of flour samples turned, not very surprisingly, out well and in some aspects even beyond expectations. TOFS was a good method to use for the evaluation of compressed flour samples and the result was satisfying. Objections could be raised against the number of measurements performed, since no confidence intervals for the different compressions could be constructed. The conclusion was that the gain of making confidence intervals was not big enough compared with the effort required. The compression method also had its limitations and drawbacks, and as a remark for the future a suggestion is to use weights of fixed masses instead of a scale.

Regarding the grains measured with time-of-flight spectroscopy the results were not as convincing. It turned out to be very hard to make the samples as similar to each other as was required to reproduce the results. Since the granules were so large, rather large spaces of air arose in between them, making it hard to know for sure if the light took a path inside grains, or if it chose to travel through the air. To improve this result a new way of preparing the samples is definitely needed. A sample holder like the one FOSS produces, but thinner, and preferably with the ability to compress the sample even further, to suppress the air spaces as much as possible, would be a lot better, and would probably improve the results considerably. Another source of error regarding the grains was the evaluation method, of which validity may be discussed, since the material consisted of big granules. Unfortunately no better alternative method exists.

The simulation of the reflection instrument, used to analyse flour, was adjusted to reproduce the absorbance of an uncompressed flour sample. To choose an uncompressed sample was maybe a mistake from the beginning, since those were harder to reproduce than those with some pressure added. It would probably be more advantageous to adjust the simulations to a sample with a small compression. But still the TOFS-measurements together with the simulations gave results reasonably similar compared with the reality, i.e. the XDS-measurements.

FOSS would be interested in using simulations to see effects of e.g. moving the sample a small distance, changing the brightness of the light source or changing the thickness of the sample. Today they modify their instruments and perform large

amounts of test measurements, in order to find out how the optimal instrument is constructed. This procedure requires a lot of time and work, but with reliable simulations it would not be necessary, and much time could be saved.

As a method, time-of-flight spectroscopy together with simulations would be usable for FOSS to evaluate how different disturbances affect the absorbance spectra, considering the flour. At the moment the simulation results are not really good enough for this, since the absolute values of reality and simulations do not fully agree. With further fine adjustments, and perhaps using a more complex model, it would be possible to use. For the grains the situation is more uncertain. Neither the shape of the simulated curves, nor the values agree properly. The simulation of wheat was closest to the real result, and could maybe, with better sample holders, and probably more advanced simulations, lead to something useful, but a lot more work is required to reach that goal.

There are many possible reasons to why the flour simulations do not give perfect results. One answer could be that the XDS-measurements were made in reflectance mode, and the TOFS-measurements in transmission mode. The sample did not have the same thickness in every measurement either; it was the pressure that was kept constant. It was also not the same physical sample that was examined in TOFS- and XDS-measurements respectively. It was the same flour, but it had been poured in and out of sample holders and thus the structure was not the same, and the two instruments were placed in two different rooms, in two different cities. The flour had thus to be transported between the two measurement locations, and e.g. humidity could have affected it. To get completely correlated data the two instruments would need to be standing next to each other in the same room, not to change the environment of the sample, and the measurements should then be performed in connection with each other, in order not to change the sample.

The same reasoning is valid also for the grain simulations, with addition that the whole method was a long shot regarding this kind of media. Both the time-of-flight measurements and the simulations turned out worse for the grains than for the flour. It was not possible to come up with an idea of what differed between the normal and the strange barley sample. There is a difference, which should be possible to detect also with time-of-flight spectroscopy, but at the moment the uncertainty of the measurements are too big. With better sample preparation and equipment, leading to a higher reproducibility, maybe an answer could be revealed.

Chapter 8

Acknowledgements

I have enjoyed working with this project very much and I would like to thank FOSS and my supervisor Christoffer Abrahamsson for coming up with the idea of the project, and letting me working with it.

I would also like to thank the Institution of Atomic Physics and my supervisor, Stefan Anderson-Engels for making the project possible to carry out. My co-supervisor, Erik Alerstam also deserves a big thank for helping me out in the lab and with the setups. And of course I thank all my supervisors for their willingness to share their knowledge and help out during the course of the project..

Bibliography

[1] Tomas Svensson. *Pharmaceutical and Biomedical Applications of Spectroscopy in the Photon Migration Regime.* PhD thesis, Division of Atomic Physics, Department of Physics, Faculty of Engineering, LTH, Lund University, 2008. p. 35-36.

[2] Website of FOSS. http://www.foss.dk/aboutfoss.aspx. 15 Jan 2009.

[3] Atomfysik: Biophotonics. http://www.atomic.physics.lu.se/biophotonics/. 15 Jan 2009.

[4] Marcelo Soto Thompson. *Photodynamic Therapy Utilizing Interstitial Light Delivery Combined with Spectroscopic Methods.* PhD thesis, Department of Physics, Lund Institute of Technology, 2004. p. 4-5.

[5] Tomas Svensson. *Pharmaceutical and Biomedical Applications of Spectroscopy in the Photon Migration Regime.* PhD thesis, Division of Atomic Physics Department of Physics, Faculty of Engineering, LTH, Lund University, 2008. p.19-22.

[6] Johannes Swartling. *Biomedical and Atmospheric Applications of Optical Spectroscopy in Scattering Media.* PhD thesis, Lund Institute of Technology, 2002. p. 23-24.

[7] Tomas Svensson. *Pharmaceutical and Biomedical Applications of Spectroscopy in the Photon Migration Regime.* PhD thesis, Division of Atomic Physics Department of Physics, Faculty of Engineering, LTH, Lund University, 2008. p. 4-5.

[8] Michael I. Mishchenko, Larry D. Travis, and Andrew A. Lacis. *Scattering, Absorption and Emission of Light by Small Particles.* Cambridge University Press, http://www.giss.nasa.gov/ crmim/books.html, third electronic release edition, 2002. 20 Jan 2009.

[9] Christoffer Abrahamsson. *Time-Resolved Spectroscopy for Pharmaceutical Applications.* PhD thesis, Department of Physics, Lund Institute of Technology, 2005.

[10] Daniele Contini, Fabrizio Martelli, and Giovanni Zaccanti. Photon migration through a turbid slab described by a model based on diffusion approximation. *Applied Optics*, 36(19):4587–4599, July 1997.

[11] Marcelo Soto Thompson. *Photodynamic Therapy Utilizing Interstitial Light Delivery Combined with Spectroscopic Methods.* PhD thesis, Department of Physics, Lund Institute of Technology, 2004. p. 19.

[12] Johannes Swartling. *Biomedical and Atmospheric Applications of Optical Spectroscopy in Scattering Media.* PhD thesis, Lund Institute of Technology, 2002. p. 34-36.

[13] Tomas Svensson. *Pharmaceutical and Biomedical Applications of Spectroscopy in the Photon Migration Regime*. PhD thesis, Division of Atomic Physics Department of Physics, Faculty of Engineering, LTH, Lund University, 2008. p. 27-29.

[14] Stefan Andersson-Engels. Course material, tissue optics. http://www-atom.fysik.lth.se/MedOpt/, 2008, 26 Jan 2009.

[15] Michael S. Patterson, Stefan Andersson-Engels, Brian C. Wilson, and Ernest K. Osei. Absorption spectroscopy in tissue-simulating materials: a theoretical and experimental study of photon paths. *Applied Optics*, 34(1):22–30, 1995.

[16] Fianium Ltd. Manual for femtopower 1060, tunable supercontinuum source, sc450-aotf.

[17] Rüdiger Paschotta. http://www.rp-photonics.com/supercontinuum(underscore) generation.html. *Encyclopedia of Laser Physics and Technology*, 9 March 2009. 10 March 2009.

[18] Claudete Fernandes Pereira, Fabiano Barbieri Gonzaga, and Celio Pasquini. Near-infrared spectropolarimetry based on acousto-optical tunable filters. *Anal. Chem.*, 80:3175–3181, 2008.

[19] B.E.A. Saleh and M.C. Teich. *Fundamentals of Photonics*. John Wiley & Sons, Inc., 1991. p. 823.

[20] Tomas Svensson and Christoffer Abrahamsson. Time resolved spectroscopy - laboratory exercise, tissue optics, lund institute of technology,. *http://www-atom.fysik.lth.se/MedOpt/*, 2008. 3 Feb 2009.

[21] Tomas Svensson, Johannes Swartling, Paola Taroni, Alessandro Torricelli, Pia Lindblom, Christian Ingvar, and Stefan Andersson-Engels. Characterization of normal breast tissue heterogeneity using time-resolved near-infrared spectroscopy. *Physics in Medicine and Biology*, 50:2559–2571, 2005.

[22] Rüdiger Paschotta. http://www.rp-photonics.com/fibers.html. *Encyclopedia of Laser Physics and Technology*, 6 Sep 2008. 10 Feb 2009.

[23] Rüdiger Paschotta. http://www.rp-photonics.com/numerical(underscore)aperture.html. *Encyclopedia of Laser Physics and Technology*, 1 Jul 2008. 10 Feb 2009.

[24] The Australian National University Website of Department of Physics. http://www.anu.edu.au/physics/new/commercial/notes/acceptance20numerical 2009. 9 Feb 2009.

[25] Rüdiger Paschotta. http://www.rp-photonics.com/multimode(underscore)fibers.html. *Encyclopedia of Laser Physics and Technology*, 6 Sept 2008. 12 May 2009.

[26] T. L. J. Chan, J. E. Bjarnason, A. W. M. Lee, M. A. Celis, and E. R. Brown. Attenuation contrast between biomolecular and inorganic materials at terahertz frequencies. *Applied Physics Letters*, 85(13):2523–2525, 2004.

[27] Aparajita Bandyopadhyay, Amartya Sengupta, Robert B. Barat, Dale E. Gary, John F. Federici, Minghan Chen, and David B. Tanner. Effects of scattering on thz spectra of granular solids. *International Journal of Infrared and Millimeter Waves*, (28):969–978, 2007.

[28] Thermo Fisher Scientific Inc. http://www.thermo.com/com/cda/resources/resources (underscore)detail/1,2166,13465,00.html. 2009. 29 April 2009.

[29] Christoffer Abrahamsson. *Time-Resolved Spectroscopy for Pharmaceutical Applications.* PhD thesis, Department of Physics, Lund Institute of Technology, 2005. p. 9.

[30] FOSS Dedicated analytical solutions. http://www.foss.dk/solutions/productsdirect/ infratecsofia.aspx. 26 May 2009.

[31] FOSS Dedicated analytical solutions. http://www.foss.dk/solutions/(tilde)/media/ files/solutions/datasheets/xdsbiodiesel/datasheetxdsbiodieselgb.ashx. *Product sheet*, 2008. 12 March 2009.

Appendix A

Expressions for Time-Resolved and Spatially Resolved Reflectance and Transmittance [10]

Time-Resolved Reflection:

$$R(\bar{r},t) = -\frac{exp\left(-\mu_a ct - \frac{\bar{r}^2}{4Dct}\right)}{2\left(4\pi Dc\right)^{3/2} t^{5/2}} \times \sum_{m=-\infty}^{+\infty} \left[z_{3,m} exp\left(-\frac{z_{3,m}^2}{4Dct}\right) - z_{4,m} exp\left(-\frac{z_{4,m}^2}{4Dct}\right)\right]$$

Time-Resolved Transmittance:

$$T(\bar{r},t) = \frac{exp\left(-\mu_a ct - \frac{\bar{r}^2}{4Dct}\right)}{2(4\pi Dc)^{3/2} t^{5/2}} \times \sum_{m=-\infty}^{+\infty} \left[z_{1,m} exp\left(-\frac{z_{1,m}^2}{4Dct}\right) - z_{2,m} exp\left(-\frac{z_{2,m}^2}{4Dct}\right)\right]$$

Spatially Resolved Reflectance:

$$\begin{aligned} R(\bar{r}) = -\frac{1}{4\pi} \sum_{m=-\infty}^{+\infty} \Bigg(& z_{3,m} \left(\bar{r}^2 + z_{3,m}^2\right)^{-3/2} \times \left\{ 1 + \left[\frac{\mu_a \left(\bar{r}^2 + z_{3,m}^2\right)}{D} \right]^{1/2} \right\} \\ & \times exp\left\{ - \left[\frac{\mu_a \left(\bar{r}^2 + z_{3,m}^2\right)}{D} \right]^{1/2} \right\} - z_{4,m} \times \left(\bar{r}^2 + z_{4,m}^2\right)^{-3/2} \\ & \times \left\{ 1 + \left[\frac{\mu_a \left(\bar{r}^2 + z_{4,m}^2\right)}{D} \right]^{1/2} \right\} \times exp\left\{ - \left[\frac{\mu_a \left(\bar{r}^2 + z_{4,m}^2\right)}{D} \right]^{1/2} \right\} \Bigg) \end{aligned}$$

Spatially Resolved Transmittance:

$$T(\bar{r}) = \frac{1}{4\pi} \sum_{m=-\infty}^{+\infty} \left(z_{1,m} \left(\bar{r}^2 + z_{1,m}^2\right)^{-3/2} \times \left\{ 1 + \left[\frac{\mu_a \left(\bar{r}^2 + z_{1,m}^2\right)}{D} \right]^{1/2} \right\} \right.$$
$$\times exp \left\{ - \left[\frac{\mu_a \left(\bar{r}^2 + z_{1,m}^2\right)}{D} \right]^{1/2} \right\} - z_{2,m} \times \left(\bar{r}^2 + z_{2,m}^2\right)^{-3/2}$$
$$\left. \times \left\{ 1 + \left[\frac{\mu_a \left(\bar{r}^2 + z_{2,m}^2\right)}{D} \right]^{1/2} \right\} \times exp \left\{ - \left[\frac{\mu_a \left(\bar{r}^2 + z_{2,m}^2\right)}{D} \right]^{1/2} \right\} \right)$$

where:

$$\begin{cases} z_{1,m} = d\,(1-2m) - 4mz_e - z_0 \\ z_{2,m} = d\,(1-2m) - (4m-2)\,z_e + z_0 \\ z_{3,m} = -2md - 4mz_e - z_0 \\ z_{4,m} = -2md - (4m-2)\,z_e + z_0 \end{cases}$$

$z_e = {}^{2}/_{\mu_s'}$

$z_0 = {}^{1}/_{\mu_s'}$

$m = 0, \pm 1, \pm 2 \ldots$ is counting the number of dipoles used

$d =$ the thickness of the slab

$D = {}^{1}/_{3\mu_s'}$

$c =$ speed of light in the medium $[{}^{m}/_{s}]$

$\bar{r} =$ horizontal distance between the fibres $[m]$

$\mu_a =$ absorption coefficient $\left[m^{-1}\right]$

$\mu_s' =$ reduced scattering coefficient $\left[m^{-1}\right]$